

NPS ARCHIVE

1999.06

KIRKPATRICK, G.

DUDLEY KNOX LIBRARY
NAVAL POSTGRADUATE SCHOOL
MONTEREY CA 93943-5101

Fretting Fatigue Analysis and Palliatives

by

Gary W. Kirkpatrick

B.S., Civil Engineering

Case Western Reserve University, 1990

Submitted to the Departments of Ocean Engineering and Materials Science and
Engineering in partial fulfillment of the requirements for the degrees of
Naval Engineer

and

Master of Science in Materials Science and Engineering

at the

Massachusetts Institute of Technology

June 1999

© 1999 Massachusetts Institute of Technology 1999. All rights reserved.

Fretting Fatigue Analysis and Palliatives

by

Gary W. Kirkpatrick

Submitted to the Departments of Ocean Engineering and Materials Science and Engineering
on 7 May 1999, in partial fulfillment of the
requirements for the degrees of
Naval Engineer
and
Master of Science in Materials Science and Engineering

Abstract

The deleterious effects of fretting on the fatigue properties of a material have been known since the work of Warlow-Davies in 1941. However, a widely accepted fretting fatigue life prediction method still does not exist and debates persist as to what the critical parameter(s) for fretting fatigue are. This work demonstrates that the surface stresses due to contact can be used to characterize the damaging effects of fretting on the fatigue properties of a material.

The elastic stress analysis performed by Hamilton for a sphere on flat plane fretting geometry is used to determine the stresses due to contact for various experimental conditions provided in previous work. It is shown that the specimen fretting fatigue life is directly related to the surface stresses induced in the material by fretting.

Fretting fatigue life prediction methods are analyzed. The stress-life approach, which is widely used in industry, is examined for its applicability for fretting fatigue conditions. The damage tolerant approach is used to determine the relative magnitudes of the crack nucleation and long crack propagation stages of fretting fatigue life.

An analysis of fretting fatigue palliatives, focusing on shot peening and coatings, is presented. A systematic method to determine the optimum shot peening depth for fretted components is proposed. The method uses the elastic stress field expressions derived by Hamilton for a sphere on flat surface contact geometry and is demonstrated for Ti-6Al-4V. However, the method is general and can be applied for any material and any contact geometry which allows analytic evaluation of the stress fields.

Thesis Supervisor: Subra Suresh

Title: Richard P. Simmons Professor of Materials Science and Engineering
Professor of Mechanical Engineering

Contents

1	Introduction	10
1.1	Definitions and Background	10
1.2	Motivation and Objectives	12
2	Review of Sphere on Flat Plane Contact Mechanics	15
2.1	Introduction	15
2.2	Hertzian Contact	15
2.2.1	Sliding Elastic Sphere on a Flat Surface	16
2.2.2	Partial Sliding	17
2.3	Hamilton's Analysis	18
3	Experimental Results	24
3.1	Introduction	24
3.2	Al 7075-T6 Experimental Results	24
3.3	Ti-6Al-4V Experiments	31
3.4	Experimental Observations	33
3.4.1	Al 7075-T6	34
3.4.2	Ti-6Al-4V	37
4	Fretting Fatigue Life Prediction Analysis	42
4.1	Introduction	42
4.2	Total Life Approach	44
4.3	Damage Tolerant Approach	51

4.3.1	Al 7075-T6	51
4.3.2	Ti-6Al-4V	55
5	Palliatives	58
5.1	Introduction	58
5.2	Shot Peening	58
5.2.1	Material Yielding Analysis	63
5.2.2	Depth of Yielding	65
5.2.3	Maximum Principal Stress Analysis	69
5.2.4	Integrated Yielding and Maximum Principal Stress Analysis (Optimum Shot Peening Depth)	70
5.3	Stress Intensity Range Threshold Analysis	74
5.4	Protective Coatings	74
6	Conclusions and Future Work	77
6.1	Conclusions	77
6.2	Future Work	78
A	Ti-6Al-4V Yielding Analysis Program	80
B	Depth of Yielding Analysis	85
C	Maximum Principal Stress Analysis	90
D	Hamilton's Expressions	94
D.1	Normal Load Stresses	94
D.2	Tangential Load Stresses	95

List of Figures

1-1	Simplified schematic of bridge type fretting pads.	12
2-1	(a) Fretting contact between a sphere and a flat surface. (b) Top view showing circular contact region and stick zone, c	16
2-2	Contact stresses at the surface due to a sphere sliding on a flat surface for Al 7075-T6.	20
2-3	Contact stresses due to a sphere sliding on a flat surface for Al 7075-T6, $z = 20$ μm	20
2-4	Plot demonstrating the effects of stick-slip conditions on σ_x for Al 7075-T6 ($c/a = 0.5$).	22
3-1	Simplified diagram of the fretting fatigue testing apparatus.	25
3-2	Plot of effective stress due to contact versus number of cycles to failure for $\sigma_b \simeq 83$ MPa.	28
3-3	Number of cycles to failure versus σ_b , $S - N$ curve for constant contact load conditions.	30
3-4	Plot of the knock-down factor versus effective stress due to contact for Al 7075-T6.	32
3-5	Plot of effective stress due to contact versus number of cycles to failure for Ti-6Al-4V ($\sigma_b \simeq 300$ MPa).	34
3-6	Picture of the left fretting pad used for test 33 with the approximate size of the stick zone shown (Al 7075-T6).	35
3-7	Picture of the left side of the specimen used for test 33 with the approximate size of the stick zone shown (Al 7075-T6).	37

3-8	Picture of cracking on the left fretting pad used for test 32 with the approximate circular area of contact shown (Al 7075-T6).	38
3-9	Picture of the left fretting pad used for test 5 (Ti-6Al-4V).	39
3-10	Picture of the left side of the specimen used for test 5 (Ti-6Al-4V).	40
3-11	Picture of cracking in the right fretting pad used for test 2 (Ti-6Al-4V).	41
4-1	Comparison of the S-N curves for plain fatigue and fretting fatigue for Al 7075-T6 ($\sigma_{ec} = 337$ MPa).	43
4-2	Plot of the Fretting Correction Factor, F versus the effective stress due to contact, $\sigma_b = 83$ MPa.	47
4-3	Plot of F versus applied bulk stress, while maintaing constant contact loads for Al 7075-T6 ($\sigma_{ec} = 337$ MPa).	47
4-4	Plot of the combination of bulk and contact loading above which fretting fatigue failure will occur for Al 7075-T6.	48
4-5	Revised plot of F versus σ_{ec} for Al 7075-T6, $\sigma_b = 83$ MPa.	49
4-6	Plot of the predicted behavior of F versus σ_{ec} for various bulk loadings (Al 7075-T6).	50
4-7	Plot of F versus σ_{ec} for Ti-6Al-4V ($\sigma_b \simeq 300$ MPa).	51
4-8	Diagram showing the elliptical crack geometry.	53
5-1	Plot showing approximate relationship between shot peened and unpeened specimens for plain and fretting fatigue.	59
5-2	Typical stress profile after shot peening and the assumed stress profile used in this work.	61
5-3	Residual stress equilibrium diagram.	61
5-4	Diagram showing the detrimental effects of shot peening if the residual stresses are relieved [44].	62
5-5	The combination of contact and bulk loading which causes the total effective stress to equal the yield stress plotted versus the coefficient of friction.	65
5-6	Plot of yielding depth, z versus maximum contact pressure for various bulk loadings ($\mu = 1.0$).	66

5-7	Depth of yielding versus maximum contact pressure for various bulk stresses ($\mu = 0.8$).	67
5-8	Depth of yielding versus maximum contact pressure for various bulk stress load- ings ($\mu = 0.5$)	68
5-9	Depth of yielding versus maximum contact pressure for various bulk stress load- ings ($\mu = 0.3$)	68
5-10	The depth at which the maximum principle stress is less than or equal to zero plotted versus maximum contact pressure, for magnitudes of bulk stress ($\mu = 1.0$). 70	
5-11	The depth at which the maximum principal stress is less than or equal to zero plotted versus maximum contact pressure for various magnitudes of bulk stress ($\mu = 0.8$).	71
5-12	The depth at which the maximum principal stress is less than or equal to zero plotted versus the maximum contact pressure for various magnitudes of bulk stress ($\mu = 0.5$).	71
5-13	Optimum peening depth plotted versus maximum contact pressure for $\mu = 1.0$ and $\sigma_b = 0.4\sigma_Y$	73
5-14	Optimum peening depth plotted versus maximum contact pressure for $\mu = 0.8$, $\sigma_b = 0.1\sigma_Y$	73
5-15	Comparison of the required peening depths for the maximum principal stress analysis and the threshold stress intensity range analysis.	75

List of Tables

2.1	Properties of 7075-T6 aluminum alloy	19
3.1	Al 7075-T6 fretting fatigue experiments	26
3.2	Al 7075-T6 Constant Bulk load data analysis	27
3.3	Stress variation as the normal load changes for a constant maximum tangential load.	29
3.4	Al 7075-T6 stress analysis for constant contact loading	30
3.5	Data used to plot the knock-down factor curve.	31
3.6	Ti-6Al-4V material properties.	32
3.7	Test parameters for Ti-6Al-4V fretting fatigue tests	32
3.8	Ti-6Al-4V stress analysis	33
3.9	Comparison of the analytical versus actual values for the fretting geometry, Al 7075-T6 (* indicates value could not be determined).	36
3.10	Comparison of the analytical versus actual fretting geometry (Ti-6Al-4V).	39
4.1	The necessary data to determine F and its relationship with the contact stresses.	46
4.2	Fretting correction factors for different bulk stresses, constant contact loads.	46
4.3	Values used in the Paris life calculations for Al 7075-T6. Consistent units for C are meters and MPa.	54
4.4	Long crack propagation life for Al 7075-T6.	56
4.5	Values used for the propagation life calculations for Ti-6Al-4V.	57
4.6	Values of C and m for STOA, Bi-modal Ti-6Al-4V and Bi-modal Ti-6Al-4V (units are meters and MPa).	57

4.7	Ti-6Al-4V long crack propagation life.	57
5.1	Parameters and respective values for the threshold stress intensity range analysis.	74

Chapter 1

Introduction

1.1 Definitions and Background

Fretting fatigue generally refers to the degradation of the fatigue properties of a material due to cyclic relative displacement between two contacting materials. The most severe impact on the fatigue properties occurs when displacement amplitudes are 10-50 μm [21]. The fretting action produces considerable wear damage to the material and also produces very large contact stresses. The reduction in fatigue life under these circumstances can be quite significant. The National Materials Advisory Board [1] gives the following definitions.

- **Fretting** . Fretting is a surface damage phenomenon occurring on two contacting surfaces having oscillatory relative motion of small amplitude.
- **Fretting-Initiated Fatigue** . A condition where the material fatigue strength is degraded by the presence of the following:
 1. Surface stress concentrations resulting at sites of fretting pits.
 2. Surface and subsurface stresses resulting from rubbing friction contact combined with the stresses resulting from the overall fluctuating stress field.

There are many practical examples of structures in which fretting occurs. These structures include: bolted and riveted joints, suspension cables, metallic coil ropes, key-way shaft couplings, coil wedges of generator rotors and blade dovetail contact sections of turbine engines

[2]. The fretting problem is made worse by the fact that many of the structures that undergo fretting cannot be easily inspected. The first detection of a crack may be when the structure fails.

The first reported observation of the occurrence of fretting during fatigue testing was made by Eden, Rose, and Cunningham [3] in 1911. They observed corrosion in the holders of the fatigue test specimens. The corrosion was such that they had difficulty removing the broken test specimens from the testing apparatus for the heavily loaded tests which lasted for several days. Eden, Rose, and Cunningham [3] also recorded the first attempt of the use of palliatives for fretting fatigue. They oiled the fatigue specimens before putting them in place, however they reported that this was only partially effective. The specimens were easier to remove, but corrosion products were still produced. The tests conducted by Eden *et al* [3] were not fretting fatigue tests, the observed fretting was noted but not analyzed.

According to Hoepfner [4] the first systematic investigation of fretting was performed by Tomlinson in 1927, in which he determined that surface damage was related to the relative displacement between the contacting surfaces. Warlow-Davies [5] investigated the impact of fretting on the fatigue properties of a material in 1941 and demonstrated that fretting reduced fatigue strength. He did not perform fretting and fatigue tests simultaneously, but fretted the specimens and then performed fatigue tests on the fretted specimens. Warlow-Davies performed the tests on medium-carbon steel and for a nickel-chromium-molybdenum alloy steel. The loss in fatigue strength after fretting was found to be 13 percent and 18 percent respectively. By separating the fretting and fatigue portions of the test, Warlow-Davies was able to measure the reduction in fatigue strength due only to the surface damage caused by fretting. Later research, such as that conducted by Waterhouse [29], showed that simultaneous fretting and fatigue resulted in much higher reductions in fatigue strength. There have been numerous other experiments demonstrating the deleterious effects of fretting on fatigue strength. Birch [11], Szolwinski & Farris [30] and Adibnazari & Hoepfner [15] are just a few of the other works that have also demonstrated the damaging effects of fretting on fatigue life.

Much work has been performed in fretting fatigue since the investigation conducted by Warlow-Davies. This thesis will not attempt to reference all the major work performed in the area of fretting fatigue. Hoepfner in [4] provides a historical review on fretting fatigue

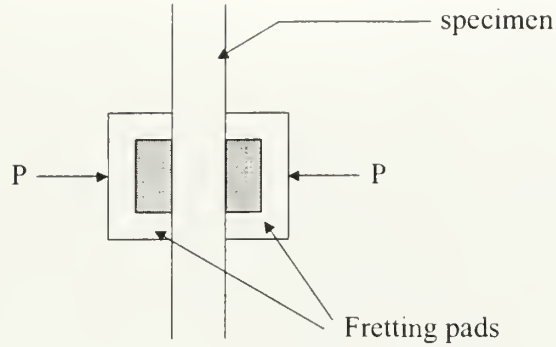


Figure 1-1: Simplified schematic of bridge type fretting pads.

research as well as a brief review of the current state of knowledge, which is part of an entire work devoted to the topic of fretting fatigue. Birch [11] also provides a brief summary of fretting research.

1.2 Motivation and Objectives

Although the damaging effects of fretting on the fatigue properties of a material have been reported quite extensively since the work of Warlow-Davies, there is still not a consensus on the critical parameter(s) for fretting fatigue. Waterhouse [9] states that the main factor in producing fatigue failure is the additional shear stress in the contact region caused by the frictional forces between the contacting bodies, while Nishioka and Hirakawa [10] stress the importance of the relative slip amplitude and Adibnazari and Hoepfner [15] demonstrate the importance of the normal pressure on fretting fatigue life. According to Birch [11], Beard lists more than fifty parameters of concern for fretting fatigue. The lack of consensus on the critical fretting parameter(s) is likely due to the experimental configurations that have been used in the past. Many of the past fretting fatigue experiments have been performed using bridge type pads as shown in Figure 1-1.

The bridge pads produce stress singularities at the contact edges making a stress analysis very difficult. Many of the experimental configurations in the past also lacked the ability to measure all of the fretting parameters, specifically the oscillating tangential contact load,

which is a very important fretting parameter. If the oscillating tangential load is not present, the problem becomes an indentation problem and not fretting. This inability to measure the contact load conditions again limited the information available for analysis. The first objective of this work is to determine the critical fretting fatigue parameter(s).

The limitations discussed above are not in this work. The work of Birch [11] and the ongoing experimental work of Conner [12] provide the experimental data used in this work. The testing apparatus used by Birch and Conner employed spherical fretting pads. The spherical fretting pads allow analytical expressions for the stress field due to contact to be determined, which was first done by Hamilton and Goodman [13]. The testing apparatus used by Birch and Conner, described in detail in [25], allows measurement of all the fretting parameters required to determine the stress fields due to contact. The expressions given in [13] were expressed again later by Hamilton [14] in a more convenient explicit form. The form developed by Hamilton [14] is implemented in this work. Hamilton and Goodman provide the elastic stress fields. This does not present a problem in this work as the stresses remained in the elastic region for all but a few tests.

The expressions given by Hamilton [14] are for a global sliding contact, which is not the condition for most of the experiments analyzed in this work. Most of the tests analyzed in this thesis have slip/stick conditions. Chivers and Gordelier [16] show how the Hamilton expressions must be modified to accommodate slip/stick fretting conditions. This modification has been implemented in this work for the slip/stick experimental conditions when necessary. It will be demonstrated in this work that the critical fretting parameters can be captured by one parameter, the maximum von Mises effective stress at the surface due to contact.

The second objective of this work is to analyze fretting fatigue life prediction methods using past experimental work. A widely accepted fretting fatigue life prediction method does not yet exist. The stress life approach, which is widely used in industry today, is examined for its applicability for fretted components. There have been several life prediction methods proposed for fretting fatigue, but none have utilized the stress-life approach. Edwards [6] in 1981 proposed a fretting fatigue life prediction method using linear elastic fracture mechanics. Faanes and Fernando [7] in 1994 also proposed a life prediction method using linear elastic fracture mechanics, but added a short crack correction to account for the effect of the high

stress gradient due to fretting on short crack growth. The success of linear elastic fracture mechanics applied to fretting has been limited by the difficulty in developing stress intensity factors to be used to predict short crack growth rates. Giannakopoulos, Lindley and Suresh [46] propose a method which circumvents this problem for sharp edged contacts in their crack analogue model. Szolwinski and Farris [30] in a recent paper propose a fretting fatigue life prediction method that uses the Smith-Watson-Topper expression [8] to predict the number of cycles to crack nucleation and employs linear elastic fracture mechanics to predict the long crack growth rate, thereby avoiding the short crack growth rate problem. This work will examine both the stress-life approach and the damage tolerant approach used to predict fatigue life.

The final portion of this work analyzes fretting fatigue palliatives; coatings and shot peening. Shot peening has been shown by Waterhouse [38], Bignonnet [39], and Chivers and Gordelier [41] to be an effective fretting fatigue palliative. However, a detailed analysis of the shot peening process applied to fretted components with the objective of determining the optimum peening depth has not yet been performed. Fretting produces large tensile and compressive stresses at the contact edges and both must be considered when determining the optimum peening depth. A systematic method to determine the optimum peening depth for a fretted component is given in this work, using the elastic stress field expressions provided by Hamilton. This analysis also includes the effects of changing the coefficient of friction on the optimal peening depth. The elastic stress fields due to contact will also be used to provide a brief discussion of the benefits of protective coatings for fretting fatigue.

This thesis is organized in the following manner: Chapter 2 provides a description of the sphere on flat plane contact mechanics used in this work. Chapter 3 uses the works of Hamilton [14], and Chivers and Gordelier [16] to analyze the experimental results provided by Birch [11], and Conner [12]. Chapter 4 analyzes fretting fatigue life prediction. Chapter 5 discusses fretting fatigue palliatives and provides a method to determine the optimum peening depth for a fretted component. Chapter 6 provides the conclusions from this work and suggestions for further study in work related to fretting fatigue.

Chapter 2

Review of Sphere on Flat Plane Contact Mechanics

2.1 Introduction

Before the analysis of Hamilton [14] and Chivers and Gordelier [16] is applied to experimental tests, a brief review of the sphere on flat plane contact mechanics is presented. The expressions reviewed here serve as the foundation for the analysis performed in this work. The discussion begins with the analysis conducted by Hertz in 1882.

2.2 Hertzian Contact

Over one hundred years ago Hertz analyzed the problem of normal, frictionless contacting spheres. Hertz solved for the contact pressure distribution, $p(r)$ and the circular radius of contact, a , by solving the integral equation governing the boundary conditions. The radius of contact as determined by Hertz [17] is given by:

$$a = \left\{ \frac{3\pi P R_1 R_2}{4(R_1 + R_2)} \left[\frac{1 - \nu_1^2}{\pi E_1} + \frac{1 - \nu_2^2}{\pi E_2} \right] \right\}^{1/3} \quad (2.1)$$

where E and ν are Young's Modulus and Poisson's ratio respectively and R is the radius of curvature. The indices 1,2 refer to the two contacting bodies. The solution derived by Hertz

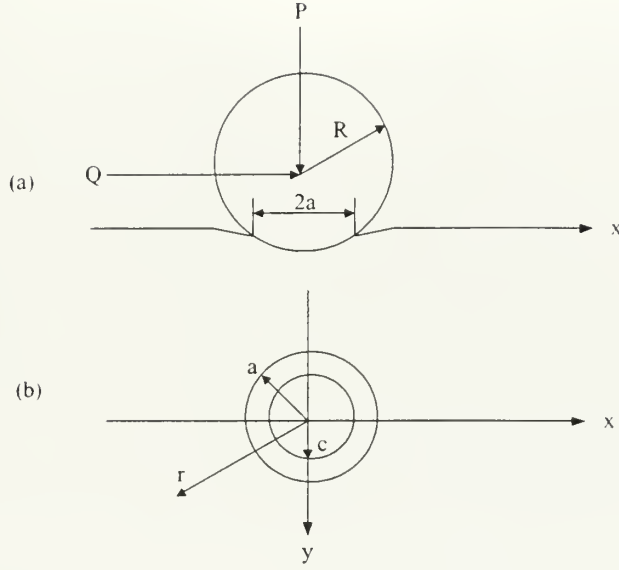


Figure 2-1: (a) Fretting contact between a sphere and a flat surface. (b) Top view showing circular contact region and stick zone, c .

for normal contacting spheres can be applied to a sphere on a flat plane geometry by noting that $\frac{1}{R_{eff}} = \frac{1}{R_{sphere}} + \frac{1}{R_{plane}}$, $R_{plane} = \infty$, therefore $R = R_{eff} = R_{sphere}$. Huber [18] in 1904, was the first to solve for the stress fields beneath the contacting surfaces.

2.2.1 Sliding Elastic Sphere on a Flat Surface

The indentation problem solved by Hertz and Huber becomes a fretting problem when an oscillatory tangential force is applied to the sphere. The problem geometry is shown in Figure 2-1.

Once the tangential force, Q , is introduced, sliding or partial slip is also introduced. The Amonton-Coulomb law relates the normal pressure and the tangential tractions, q by:

$$\frac{|q|}{p} = \frac{|Q|}{P} = \mu \quad (2.2)$$

where μ is the coefficient of kinetic friction.

As given first by Mindlin [19] in 1949 and again later by Hamilton [14] the stresses at the

contact surface for incipient sliding conditions are given by:

$$\sigma_z = \frac{-3P}{2\pi a^3} \sqrt{a^2 - r^2}, \quad 0 \leq r \leq a \quad (2.3)$$

$$\tau_{zx} = \frac{-3\mu P}{2\pi a^3} \sqrt{a^2 - r^2}, \quad 0 \leq r \leq a \quad (2.4)$$

τ_{yz} and the boundary stresses outside the circular area of contact are zero. As mentioned above, these boundary conditions only apply under conditions of gross sliding, that is when $Q = \mu P$. The expression given by Equation 2.3 is also the expression for contact pressure due to indentation without sliding and the expression given for the contact radius by Equation 2.1 is also unchanged by the addition of a tangential load. Therefore, the presence of the shear stresses on the surface has not affected either the circular contact radius or the contact pressure.

2.2.2 Partial Sliding

When the applied tangential force is less than the product of μP , macroscopic sliding does not occur, however frictional traction at the contact interface leads to small relative displacement over part of the interface. This small relative motion is commonly referred to as micro-slip. The remaining portion of the interface deforms without any relative motion. The region in which no relative motion occurs is referred to as the stick region. All the points on the surface within the stick region undergo the same tangential displacements. The stick region is shown in Figure 2-1. Mindlin [20] has shown that a stick region exists in the contact interface and the radius, c , of the outer boundary of the stick region to be given by:

$$\frac{c}{a} = \left[1 - \frac{Q}{\mu P} \right]^{1/3}, \quad c \leq r \leq a. \quad (2.5)$$

As shown in Figure 2-1, the stick region is concentric with the contact area, this geometric relationship is also observed for experimental specimens.

Just as the boundary conditions had to be reestablished for sliding, they must again be modified to account for micro-slip. The stresses at the contact surface are now given by [19]:

$$\tau_{zx} = \frac{3\mu P}{2\pi a^2} \sqrt{a^2 - r^2}, \quad c \leq r \leq a \text{ and} \quad (2.6)$$

$$\tau_{zx} = \frac{3\mu P}{2\pi a^2} \left\{ (a^2 - r^2)^{1/2} - (c^2 - r^2)^{1/2} \right\}, \quad r \leq c. \quad (2.7)$$

The expression for the normal pressure is the same as in the global sliding condition. The relative tangential displacements are given by [19]:

$$\delta = \frac{3\mu P}{16a} \left\{ \frac{2 - \nu_1}{G_1} + \frac{2 - \nu_2}{G_2} \right\} \left\{ 1 - \left(1 - \frac{Q}{\mu P} \right)^{2/3} \right\}. \quad (2.8)$$

2.3 Hamilton's Analysis

As mentioned in the previous section, the stress fields beneath the surface of a circular indenter were first derived by Huber in 1904. However, the elastic stress fields beneath the surface of a circular sliding contact on a flat surface were not derived until 1966 by Hamilton and Goodman [13]. Mindlin's work in circular sliding contact focused primarily on surface compliance and the micro-slip problem. He did not analyze the stresses below the contact surface.

It must be stressed that the equations given by Hamilton are for a global sliding sphere and not for stick/slip conditions. It was shown earlier that the boundary stresses are not the same for the two conditions. The stress equations for the global sliding condition must be modified slightly to obtain the correct stresses for situations involving micro-slip. Chivers and Gordelier [16] demonstrate how the expressions must be modified. The results of a stress analysis performed using the expressions given by Hamilton are shown in Figure 2-2. The expressions used to generate this plot are given in Appendix D. The material used to generate this plot was Al 7075-T6. Some material properties for this alloy are listed in Table 2.1 [11] [21] [22]. Spherical fretting pads with a one inch radius were used and global sliding is assumed. Using the values for μ , E , and ν in Table 2.1 and the elastic stress field equations given by Hamilton, the stresses in the x and y directions have been plotted in Figure 2-2 along with the von Mises effective stress, σ_{eff} , at $z = 0$, $y = 0$. The stresses have been normalized by the maximum contact pressure, P_0 , $P_0 = \frac{3P}{2\pi a^2}$. The von Mises effective stress parameter, σ_{eff} , has been used because this is a multiaxial problem. The *effective* stress is used to convert the multiaxial stress state to a single stress parameter. The expression for the effective stress is

Material Property	Value
Young's modulus (E)	72 GPa
Poisson ratio (ν)	0.3
Monotonic yield stress (σ_Y)	469 MPa
Coefficient of kinetic friction (μ)	1.2
Tensile strength (σ_{TS})	579 MPa
Endurance limit (σ_{end})	179 MPa
Fatigue strength coefficient (σ'_f)	1317 MPa
Fatigue strength exponent (b)	-0.126
Fatigue limit stress (σ_D)	230 MPa
Fatigue ductility coefficient (ϵ_f)	0.19
Fatigue ductility exponent (c)	-0.56

Table 2.1: Properties of 7075-T6 aluminum alloy

given by:

$$\sigma_{eff} = \frac{\left[(\sigma_x - \sigma_y)^2 + (\sigma_y - \sigma_z)^2 + (\sigma_z - \sigma_x)^2 + 6(\tau_{xy}^2 + \tau_{yx}^2 + \tau_{zx}^2) \right]^{1/2}}{\sqrt{2}}. \quad (2.9)$$

The stress fields displayed in Figure 2-2 are not the only non-zero stress fields at the surface; the shear stress τ_{zx} and the normal stresses in the z-direction are also non-zero, however they both go to zero at the contact edges. The stresses below the surface at a depth of 20 μm is plotted in Figure 2-3. Comparing Figures 2-2 and 2-3, it can be seen that the stresses due to contact quickly decay away, especially the tensile stress at the trailing edge of contact, $x = -a$, in the x-direction. From Figure 2-2 it can be seen that there is a large peak in σ_x at the trailing edge of contact. This stress is the highest stress on the plot. In Figure 2-3, the peak tensile stress at the trailing edge is much lower in magnitude and the slope of the σ_x curve is also much smoother.

The maximum von Mises effective stress is also at the surface. This is true for a sphere sliding on a flat surface when $\mu > 0.3$. When $\mu = 0$, or when the tangential force, Q , is zero, the maximum von Mises stress shifts below the surface to the point $z = 0.5a$, for $\nu = 0.3$ [14]. However, for a sphere fretting on a flat plane, the maximum von Mises and the maximum tensile stresses generally occur at the surface. Although the maximum tensile stress has a severe peak at the trailing edge of contact at the surface, the von Mises effective stress is roughly constant over a very large region as can be seen in Figure 2-2.

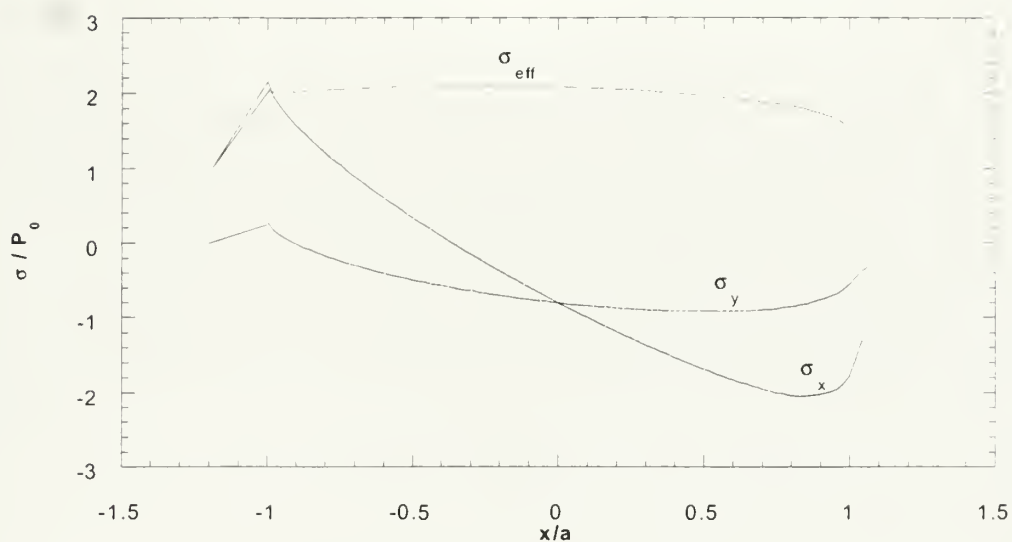


Figure 2-2: Contact stresses at the surface due to a sphere sliding on a flat surface for Al 7075-T6.

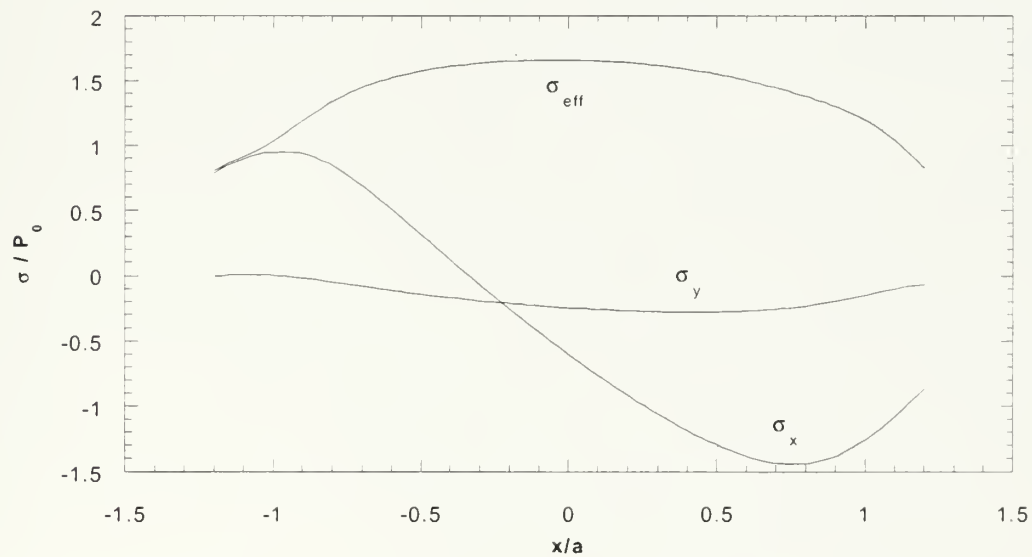


Figure 2-3: Contact stresses due to a sphere sliding on a flat surface for Al 7075-T6, $z = 20 \mu\text{m}$.

The analysis performed in this work will focus on the surface stresses, at the trailing edge of contact, with the exception of the shot peening analysis, which analyzes below the surface and inside the contact edges. The contact stresses are maximum at the surface and the maximum tensile stress occurs in the material at the trailing edge of the contact; therefore, this work will focus its analysis on this location. The von Mises effective stress is just as high at other locations on the surface, however this is in general due to large compressive stresses at that location. It is assumed that the large tensile stress is responsible for crack nucleation. The contact stresses given by Hamilton can be greatly simplified for $x = -a$, $z = 0$ and $y = 0$, the problem becomes a biaxial one. The only non-zero stresses at this location are σ_x and σ_y , and are given by:

$$\sigma_x = P_0 \left[\frac{(1-2\nu)}{3} \pm \frac{4+\nu}{8} \pi \mu \right], \quad x = \mp a, \text{ and} \quad (2.10)$$

$$\sigma_y = P_0 \left[\frac{(2\nu-1)}{3} \pm \frac{3\nu\mu}{8} \right], \quad x = \mp a. \quad (2.11)$$

Note carefully the position of the signs. The maximum tensile stress in both the x and y directions occurs at the trailing edge of contact. Again, it must be emphasized that the stresses given in equations 2.10 and 2.11 are for full sliding and not for stick/slip conditions. Figure 2-4 displays the curves for σ_x under incipient sliding and stick/slip conditions. As can be seen in this figure, when stick/slip is accounted for, σ_x is reduced for the given contact load conditions. This figure was generated using a c/a ratio of 0.5.

Recall that the ratio of c/a indicates how close to full sliding or full stick the fretting condition is. As $c/a \rightarrow 0$, global sliding is introduced, when $c/a = 1$, full stick conditions exist. From Figure 2-4, it can be seen that the magnitude of the maximum tensile stress is reduced when micro-slip is taken into consideration. This fact will become more relevant later during the shot-peening analysis of this work. The reduction in stress under stick/slip conditions is in direct conflict with experimental results. Experiments have shown that fretting is most damaging to the fatigue properties of a system under micro-slip conditions with relative displacements of 10-50 μm . The introduction of global sliding improves the fretting fatigue life. It has been postulated that this improvement under sliding conditions may be due to the wearing away of fatigue cracks from the surface, so that they do not become propagating fatigue cracks. This is one example of the limitations of the stress analysis.

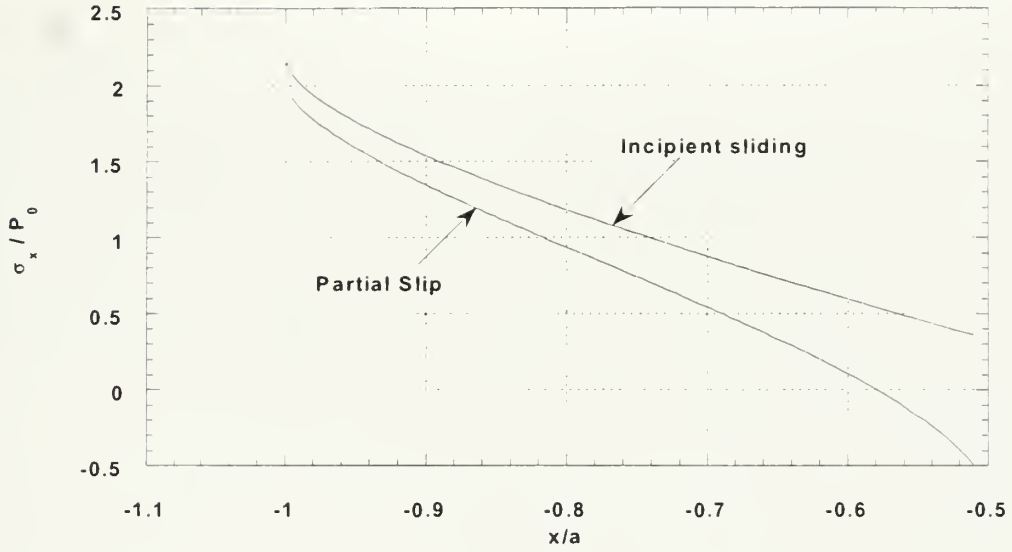


Figure 2-4: Plot demonstrating the effects of stick-slip conditions on σ_x for Al 7075-T6 ($c/a = 0.5$).

In most practical structures and scientific experiments, the tangential load, Q , which changes the problem from one of indentation to fretting, is caused by an applied cyclic bulk stress. Therefore, to perform a complete analysis, the stresses induced in the material by the bulk load must also be accounted for. If the material behaves elastically, the principle of superposition can be applied. Using superposition, the stresses at the surface, at $r = a$, are given by:

$$\sigma_{x\text{tot}} = \sigma_{xc} + \sigma_{xb} \text{ and} \quad (2.12)$$

$$\sigma_{y\text{tot}} = \sigma_{yc} + \sigma_{yb}, \quad (2.13)$$

where $\sigma_{x\text{tot}}$ and $\sigma_{y\text{tot}}$ are the total stresses in their respective directions. σ_{xc} and σ_{yc} are the contact stresses in their respective directions and σ_{xb} , σ_{yb} are the bulk stresses in the x and y directions respectively. The condition described above, that of a cyclic bulk load in combination with the applied contact loads, was the method used to produce the experimental results analyzed in this work. The bulk load also produces eccentricity in the contact geometry. The contact area and stick zone are no longer perfectly circular. This effect is discussed in

detail in [23].

Chapter 3

Experimental Results

3.1 Introduction

As shown earlier, the elastic stress fields for a sphere sliding on a flat plane are known and can be found as functions of the normal and tangential loads. The testing apparatus developed at the Massachusetts Institute of Technology gives the user the ability to control and measure both the normal and tangential contact loads. This apparatus has been used to conduct fretting fatigue tests on Al 7075-T6 and Ti-6Al-4V. The testing apparatus is described in [25]. A simplified diagram of the test setup is shown in Figure 3-1. These tests provide the necessary information to calculate the elastic stress fields due to contact, which will be discussed in detail in the following sections. The elastic stress fields at the surface due to contact do not completely describe the fretting phenomenon, there are some shortcomings. The stress analysis does not account for the condition of the surface and may not give the correct location of crack initiation. However, the stress analysis provides a very good starting point for a systematic analysis of the problem.

3.2 Al 7075-T6 Experimental Results

The experimental data provided in the work performed by Birch [11] and Conner [12] is shown in Table 3.1. Table 3.1 provides all the necessary information to calculate the stress fields. The bulk stress, σ_b , for these experiments was applied in the x-direction only, with a stress ratio,

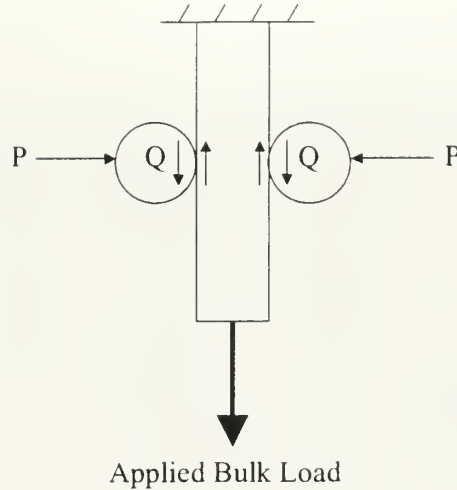


Figure 3-1: Simplified diagram of the fretting fatigue testing apparatus.

$$R = -1.$$

Care must be taken when superposing the bulk stress. As discussed earlier the trailing edge of contact is the point of interest for this analysis; however, during each complete stress cycle the trailing edge becomes the leading edge as the bulk stress is reversed. The trailing edge during the tensile portion of the bulk stress loading cycle becomes the leading edge during the compressive portion of the loading cycle. This location on the specimen undergoes the highest tensile stresses and the largest stress amplitude. The opposite edge of contact endures lower stresses because it becomes the trailing edge of contact during the compressive portion of the bulk loading cycle. It would be expected that the cracks would initiate from the edge of contact which undergoes the highest stresses. This fact is verified in [23] which displays a fretting scar with cracking visible only on one side of the circular contact region.

The loading conditions displayed in Table 3.1 were used to calculate the surface stresses at the trailing edge of contact for each test specimen. To better analyze the results of the stress analysis, this work has isolated two series of experiments, which correlate to two different loading conditions. The first series of tests includes those tests where the bulk stress was roughly constant ($\sim 83\text{MPa}$), while the contact loads were varied. Therefore, the effects of the

Test	P (N)	Q (N)	$Q/(\mu \times P)$	σ_b (MPa)	N_f (Cycles)
1	20.8	15	0.60	83	449,5500
2	30	15	0.42	85	480,000
3	15.6	15	0.80	85	395,000
4	12.5	15	1.0	83	361,000
5	18.5	13.5	0.61	77	551,000
6	16	11.7	0.61	83	530,000
7	8.75	7	0.67	83	3,300,000 (no failure)
8	13	7	0.45	83	10,680,000 (no failure)
9	13.9	10	0.60	83	803,000
10	10.3	7.5	0.61	83	2,940,000
11	7.31	6.6	0.75	83	3,450,000 (no failure)
12	8.33	8	0.80	83	616,000
13	20	15	0.63	69	1,410,000 (no failure)
14	20	21.5	0.89	54	2,186,000 (no failure)
15	20	20	0.83	61	2,500,000 (no failure)
16	24	20.25	0.70	61	2,666,000 (no failure)
17	28	20	0.59	61	2,505,000 (no failure)
18	11.5	8.6	0.62	83	2,608,000 (no failure)
19	20	15	0.63	83	549,000
20	20	15	0.63	70	516,000
21	20	15	0.63	56	1,540,000 (no failure)
22	20	15	0.63	63	2,940,000 (no failure)
23	20	15	0.63	59	1,777,000 (no failure)
24	25	23	0.77	270	297,000
25	25	22.5	0.75	270	135,000
26	22.5	19.5	0.72	230	480,000
27	20	17	0.71	195	575,000
28	20	15	0.63	75	3,050,000
29	20	15	0.63	100	390,000
30	20	15	0.63	125	258,063
31	20	15	0.63	150	181,118
32	20	15	0.63	74	2,497,226
33	20	15	0.63	67	3,200,845 (no failure)

Table 3.1: Al 7075-T6 fretting fatigue experiments

Test	a (μm)	c/a	σ_{xtot} (MPa)	σ_{ec} (MPa)	N_f (Cycles)
8	184	0.82	338	248	10,680,000 (no failure)
7	162	0.69	360	264	3,300,000 (no failure)
11	152	0.63	362	264	3,450,000 (no failure)
10	171	0.73	361	266	2,940,000
18	177	0.72	375	280	2,608,000 (no failure)
12	159	0.58	384	285	616,500
9	188	0.74	388	292	803,000
6	197	0.73	405	309	530,000
2	244	0.83	409	317	480,000
1	216	0.74	432	334	449,500
19	213	0.72	435	337	549,000
3	196	0.58	456	351	395,000
4	182	0.0	473	366	361,000

Table 3.2: Al 7075-T6 Constant Bulk load data analysis

bulk stress are the same in each test and the difference in life is due only to the difference in contact stress. The second series of tests analyzed are made up of tests with constant contact loading ($P = 20$ N, $Q = 15$ N), while the bulk stress is varied, which isolated the effect of the bulk stress on fatigue life.

The results of the stress calculations for the constant σ_b series of tests are shown in Table 3.2. Table 3.2 displays the calculated values for the contact radius, a , the ratio of the stick zone radius to the contact zone radius (c/a), the maximum tensile stress at the trailing edge of contact, σ_{xtot} and the effective stress due to contact at the trailing edge, σ_{ec} .

Table 3.2 has been arranged in order from lowest to highest σ_{ec} . Note that the fatigue lifetimes as a result are nearly arranged in order from greatest number of cycles to lowest. This fact indicates that a relationship exists between the surface stresses at the trailing edge of contact and the fretting fatigue life of the specimen. This relationship will be discussed further in the next chapter, where fretting fatigue life prediction methods are discussed. The fatigue life versus effective stress due to contact is plotted in Figure 3-2. Figure 3-2 again demonstrates the existence of a relationship between the fatigue life and the surface stresses due to contact. Recall that each one of these tests were conducted with approximately the same applied bulk load, therefore the difference in fatigue life is due to the difference in contact loading only. It can be seen that as the contact stresses are reduced, the fatigue life increases. For this bulk loading condition it appears that specimen failure will not occur if σ_{ec} is maintained less than

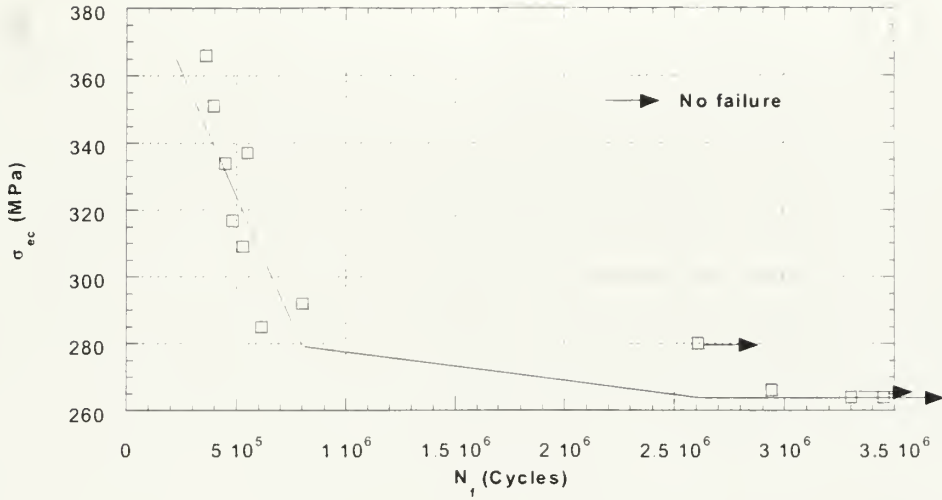


Figure 3-2: Plot of effective stress due to contact versus number of cycles to failure for $\sigma_b \simeq 83$ MPa.

about 264 MPa, which provides an endurance type stress combination. Also note that in none of the tests was the effective stress due to contact greater than the yield strength of the material; however, in test four, the total stress in the x-direction does slightly exceed the yield strength of the material.

The stress values are not the only important values displayed in Table 3.2; the values calculated for a and c/a are also quite important. They provide analytical values that can be easily checked against the actual scars on the specimens, which is done later in this chapter. This gives insight into the validity of the tests.

The value of c/a not only provides a means to verify testing procedures, it also is a key parameter in characterizing the nature of the fretting condition. Recall that as c/a goes to zero, global sliding is introduced and when $c/a = 1$, complete stick is occurring. It can be seen from Table 3.2, that in Test 4 global sliding should be occurring. The c/a value can also provide insight into the existence of a normal pressure threshold discussed by Adibnazari and Hoepfner [15]. Table 3.3 displays tests with the same value of tangential load (15N), with increasing values of normal load. It can be seen that as the normal load is increased, the maximum tensile stress and the effective stress due to contact actually decrease. Therefore, for

Test	P (N)	Q (N)	σ_{xtot} (MPa)	σ_{ec} (MPa)
4	12.5	15	473	366
3	15.6	15	456	351
14	20	15	435	337
1	20.8	15	432	334
2	30	15	409	317

Table 3.3: Stress variation as the normal load changes for a constant maximum tangential load.

a given tangential load, as the normal load is increased, the contact stresses at the trailing edge of contact decrease, and from Table 3.2 and Figure 3-2 the fretting fatigue life should increase. This provides a rational explanation of why a pressure threshold exists. The stresses decrease as the normal load is increased due to the lowering of c/a . As c/a goes to zero, the relative displacements also go to zero and complete stick results.

The results for the second series of tests, in which the contact loads were maintained constant while the bulk load was varied, are shown in Table 3.4. The data in Table 3.4 is presented in order of ascending bulk load. The values for contact radius, a and c/a are unchanged for each test, since the contact loads are identical for each test. The values of a and c/a were found to be $213 \mu\text{m}$ and 0.72 respectively. The value of c/a was <1 , therefore all the tests were conducted under stick/slip conditions. The most interesting aspect of this set of tests is the appearance of a fretting fatigue endurance type limit for the given contact conditions. It appears that when the bulk stress is reduced below approximately 70 MPa for the given contact loading conditions, specimen failure will not result. Figure 3-3 is a plot of the bulk stress versus the number of failures to cycle (S-N curve) for these contact conditions. This is not a curve with universal applications. It only applies to the contact conditions used in this set of tests. A different set of contact load conditions will result in a different endurance strength. However, combining the data from the first set of Al 7075-T6 tests with this set of data and the known endurance strength of the material a curve that does have universal applications can be proposed. This curve is shown in Figure 3-4. In this figure the so called knock-down factor, which is the factor reduction of the endurance strength of the material due to fretting, is plotted versus the effective stress due to contact at the trailing edge.

The curve displayed in Figure 3-4 is a very rough approximation of the reduction in the

Test	a (μm)	c/a	σ_{xtot} (MPa)	σ_{ec} (MPa)	N_f (Cycles)	σ_b (MPa)
21	213	0.72	408	337	1,540,000 (no failure)	56
23	213	0.72	411	337	1,777,000 (no failure)	59
22	213	0.72	415	337	2,940,000 (no failure)	63
33	213	0.72	419	337	3,200,845 (no failure)	67
13	213	0.72	421	337	1,410,000 (no failure)	69
20	213	0.72	422	337	516,000	70
32	213	0.72	426	337	2,497,226	74
28	213	0.72	427	337	3,050,000	75
19	213	0.72	435	337	549,000	83
29	213	0.72	452	337	390,000	100
30	213	0.72	477	337	258,063	125
31	213	0.72	502	337	181,118	150

Table 3.4: Al 7075-T6 stress analysis for constant contact loading

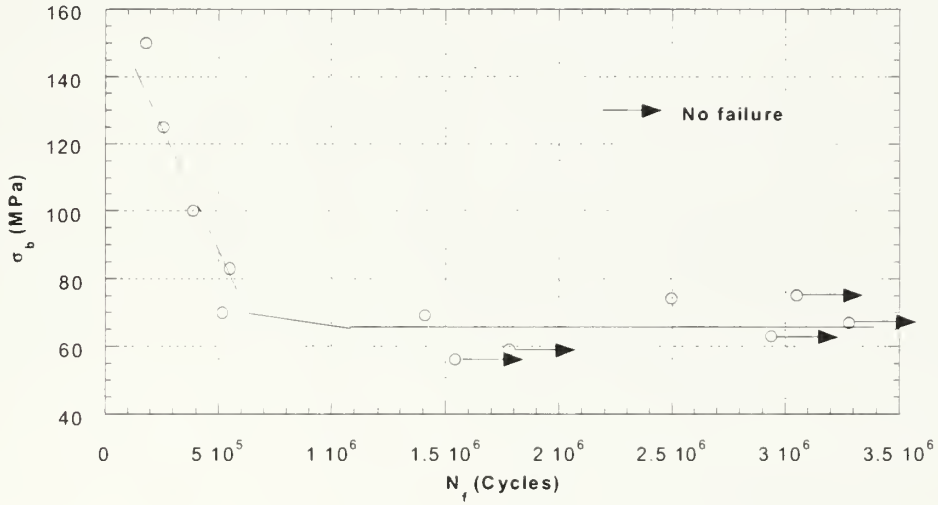


Figure 3-3: Number of cycles to failure versus σ_b , $S - N$ curve for constant contact load conditions.

σ_b (MPa)	σ_{ec} (MPa)	KF
70	337	2.51
83	264	2.12
176	0	1.0

Table 3.5: Data used to plot the knock-down factor curve.

endurance strength of the material due to fretting. The knock-down factor is given by:

$$KF = \frac{\sigma_{end}(\text{no fretting})}{\sigma_{end}(\text{fretting})}$$

where σ_{end} is the endurance strength of the material. Figure 3-4 was constructed using only three data points; several more series of tests at different bulk loads need to be performed to determine the accuracy of this plot. However, the accuracy of this plot is not the critical issue, the premise on which the plot was constructed is much more important. The plot indicates that KF is not a single number for a given material, but it can be determined if the contact stresses are known. The fact that the strength reduction changes for various contact loads can easily be seen in Figure 3-2. This idea will be examined closer in the next chapter. The data points used to make Figure 3-4 are displayed in Table 3.5. When the contact stresses go to zero, the knock-down factor goes to one.

3.3 Ti-6Al-4V Experiments

The second material analyzed in this work is Ti-6Al-4V [12]. The same test apparatus discussed earlier was also used in the Ti-6Al-4V fretting fatigue tests, utilizing the same sphere on flat surface fretting geometry. Table 3.6 provides the necessary material properties to perform the stress calculations for this material. Fuchs [22] provides fatigue properties for many different materials and was used along with [11] and [45] to produce Table 3.6.

The loading conditions used to conduct the tests on the titanium alloy are presented in Table 3.7. The results of the stress analysis are displayed in Table 3.8. The value used for the coefficient of friction was $\mu = 0.5$ for the displayed results. The fretting pad radius, R , used in these tests was 0.5 inches versus one inch used for the Al 7075-T6 tests.

A plot of the fatigue life versus the effective stress due to contact is shown in Figure 3-5.

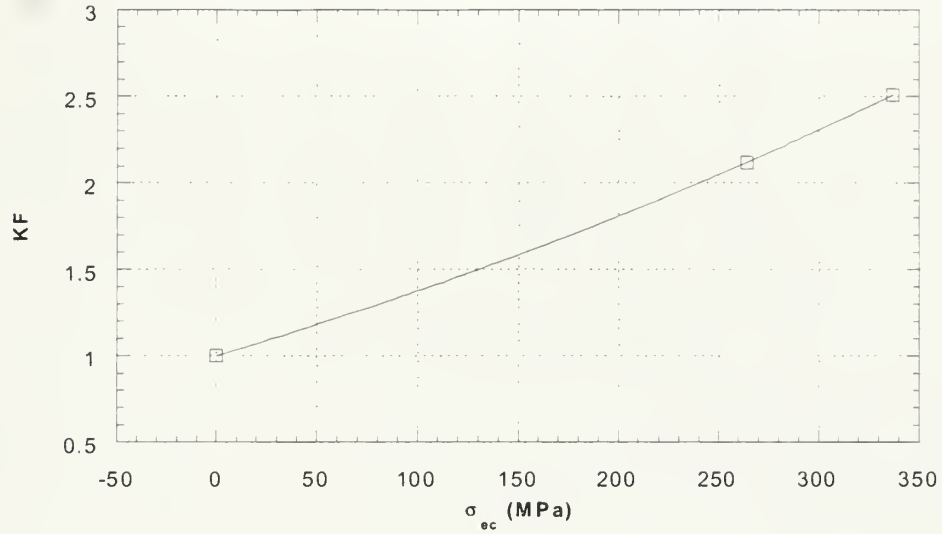


Figure 3-4: Plot of the knock-down factor versus effective stress due to contact for Al 7075-T6.

Material Property	Value
Young's Modulus (E)	115.7 GPa
Poisson ratio (ν)	0.321
Coefficient of kinetic friction	0.4-0.5
Monotonic yield stress (σ_y)	925 MPa
Endurance strength (σ_{end})	525 MPa
Fatigue strength coefficient (σ'_f)	1933 MPa
Fatigue strength exponent (b)	-0.10

Table 3.6: Ti-6Al-4V material properties.

Test	P (N)	Q (N)	$Q/(\mu \times P)$	σ_b (MPa)	N_f (Cycles)
1	50	31.5	1.26	225	691,612
2	50	23.5	0.94	400	109,574
3	50	14.5	0.58	394	107,879
4	50	13	0.52	357	31,540 (interrupted)
5	50	12.25	0.48	298	304,456
6	50	14.5	0.58	300	474,656
7	50	23	0.96	327	143,683
8	30	18	1.20	300	258,576
9	30	9	0.60	300	3,257,000 (no failure)

Table 3.7: Test parameters for Ti-6Al-4V fretting fatigue tests

Test	a (μm)	c/a	σ_{xtot} (MPa)	σ_{ec} (MPa)
1	195	0	973	714
2	195	0.39	988	567
3	195	0.75	839	448
4	195	0.78	775	426
5	195	0.80	702	414
6	195	0.75	745	448
7	195	0.43	907	564
8	164	0	904	577
9	164	0.74	682	384

Table 3.8: Ti-6Al-4V stress analysis

This figure includes tests 5-9, where the bulk stress was $\simeq 300$ MPa. Again, the fatigue life increases as the contact stresses are reduced. An endurance type limit is also seen for this material. For $\sigma_b \simeq 300$ MPa, it appears specimen failure will not occur if σ_{ec} is maintained less than about 390 MPa. More experimental tests are needed to confirm this observation. Not enough experimental data was available to plot a graph of the fretting fatigue life versus applied bulk stress.

3.4 Experimental Observations

Observations of the fretting pads and specimens have been made using a scanning laser microscope and an optical microscope. The pictures provided in this section were produced using images provided by the scanning laser microscope. The scanning laser microscope made it very simple and quick to perform accurate measurements of the fretting parameters, such as the contact radius, a and the radius of the stick zone, c .

The expressions for the contact radius, a , and the stick zone radius, c , as derived by Hertz [17] and Mindlin [19] respectively are given in Chapter 2 of this work. The analytical values for these parameters have been calculated for each test conducted on Al 7075-T6 and Ti-6Al-4V and will be compared with the actual specimen values when possible. The results of the comparison are given in the next section.

A second objective of this observational work was to determine the location of crack initiation. To achieve this objective the spherical fretting pads and the unbroken fatigue specimens

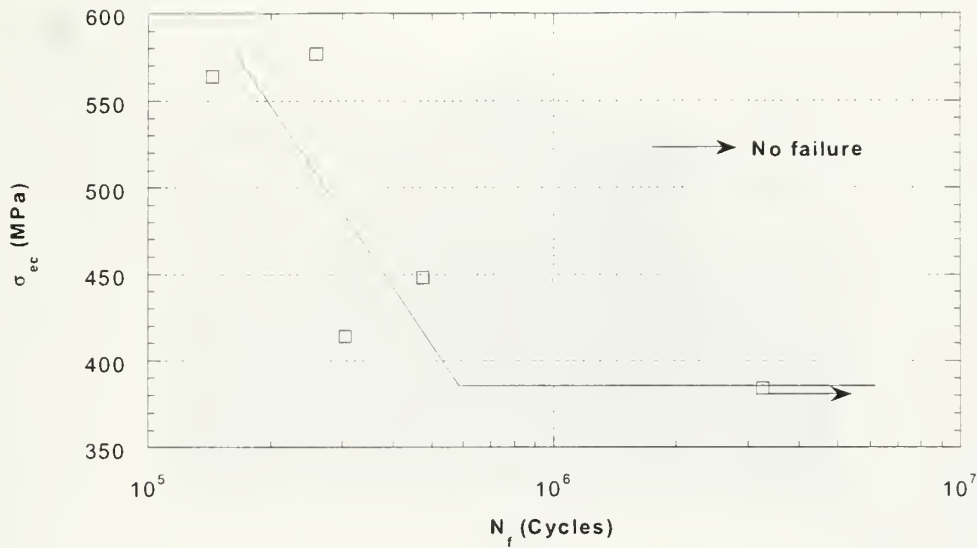


Figure 3-5: Plot of effective stress due to contact versus number of cycles to failure for Ti-6Al-4V ($\sigma_b \simeq 300$ MPa).

have been analyzed. The fretting pads provide an opportunity to see the influence of the contact stresses alone on crack initiation, due to the fact that they are not subjected to an applied bulk stress.

3.4.1 Al 7075-T6

Not all of the specimens from the 33 Al 7075-T6 tests shown in Table 3.1 were available to be analyzed, only about one-half of the tests had pads or specimens that could be analyzed. The fretting pads provided nearly all of the observations because when the specimens failed they usually failed at the fretting scar. It was very difficult to determine the fretting parameters a , and c/a for many of the pads and in some cases it could not be done. The stick and slip zones could not be distinguished for many of the pads that correspond to specimen failure. Table 3.9 shows the comparison between the predicted (Pred. in the table) and actual (Act. in the table) values for the fretting geometry, for those specimens where the comparison was possible. L and R correspond to the left and right fretting pads respectively. Test 33, which did not produce specimen failure also displays the values for the specimen and are denoted by “(spec)”

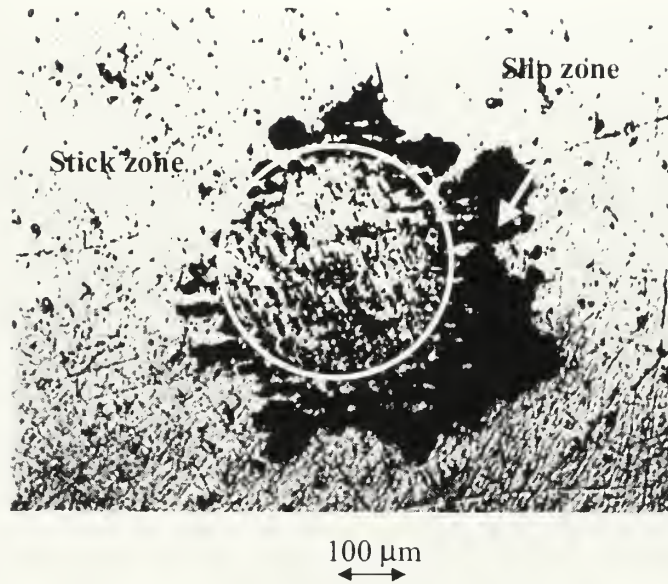


Figure 3-6: Picture of the left fretting pad used for test 33 with the approximate size of the stick zone shown (Al 7075-T6).

in the table. It can be seen from this table that the actual contact radius is in general larger than that predicted by Equation 2.1. In some cases the difference is quite substantial. The actual c/a ratios are fairly close to the predicted values, indicating that the value used for μ is accurate.

As discussed earlier, a scanning laser microscope was used to observe these specimens and to produce images of the scars. Figure 3-6 shows the fretting scar on the left pad used for test 33. The stick and slip regions are clearly evident and the eccentricity caused by the applied bulk can also be seen. The corresponding fretting fatigue specimen is shown in Figure 3-7. The fretting scar on the specimen is not as visible as the scar on the pad. The fretting geometry is not as easy to distinguish for specimens that were cycled to failure. It is difficult to determine even the contact radius of the pads for the failed specimens and nearly impossible to determine the stick zone radius.

The other objective of this section was to determine the location of cracking. No cracking was evident in Figures 3-6 and 3-7. It would have been extremely beneficial if cracking could have been observed in Figure 3-6, because the stick and slip zones are readily identifiable. As

Test	a (μm , Pred.)	a (μm , Act.)	c/a (Pred.)	c/a (Act.)	Cracking
5L	207	200	0.73	*	no
5R	207	186	0.73	*	yes
12R	159	247	0.58	*	yes
15L	213	325	0.55	*	no
15R	213	305	0.55	*	no
17L	238	248	0.74	*	no
17R	238	264	0.74	*	no
18L	177	210	0.72	*	no
19L	213	264	0.72	*	no
19R	213	249	0.72	*	no
21L	213	226	0.72	*	no
21R	213	202	0.72	*	no
22L	213	240	0.72	0.64	no
22R	213	241	0.72	0.65	no
23L	213	230	0.72	0.51	no
23R	213	225	0.72	0.67	no
28L	213	362	0.72	0.79	no
28R	213	*	0.72	*	no
29 L	213	*	0.72	*	indefinite
29 R	213	*	0.72	*	indefinite
30 L	213	*	0.72	*	yes
30 R	213	*	0.72	*	yes
31 L	213	241	0.72	0.65	yes
31 R	213	265	0.72	*	yes
32 L	213	239	0.72	*	yes
32 R	213	279	0.72	*	yes
33 L	213	238	0.72	0.61	no
33 R	213	257	0.72	0.61	no
33 L (spec)	213	253	0.72	0.69	no
33 R (spec)	213	244	0.72	0.78	no

Table 3.9: Comparison of the analytical versus actual values for the fretting geometry, Al 7075-T6 (* indicates value could not be determined).

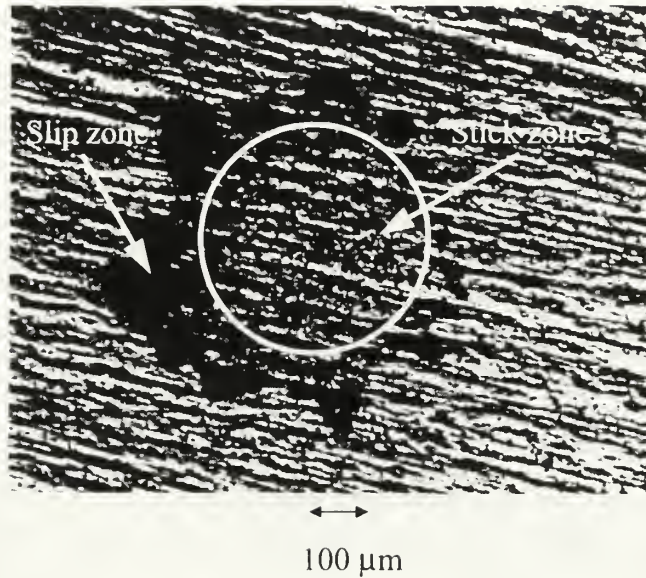


Figure 3-7: Picture of the left side of the specimen used for test 33 with the approximate size of the stick zone shown (Al 7075-T6).

Table 3.9 shows, cracking was found on eight of the fretting pads. The cracking found on the left fretting pad for test 32 is shown in Figure 3-8. The cracking is on the right side of the picture and appears to have started approximately at the edge of contact. The stick and slip zones cannot be distinguished, so the exact location of crack initiation cannot be determined from this figure. It is interesting that cracking was found on the fretting pads used for test 32, but no evidence of cracking can be found on the pads or specimen used for test 33. The two tests had exactly the same contact loading and the difference in the applied bulk stress was only 7 MPa. It would seem logical that fretting would have initiated cracking in both tests and an arrested crack would be produced in test 33 due to the lower bulk stress, but this was not found.

3.4.2 Ti-6Al-4V

The results of the observations performed on the Ti-6Al-4V test specimens are shown in Table 3.10. Again it was very difficult to observe the fretting geometry for the specimens which were cycled to failure; however, test 5 provided an interesting specimen. Even though the



Figure 3-8: Picture of cracking on the left fretting pad used for test 32 with the approximate circular area of contact shown (Al 7075-T6).

specimen was cycled to failure, the fracture surface went above the scar on the left side of the specimen and preserved the scar. The ratio of c/a was calculated using a coefficient of friction, $\mu = 0.5$, which produced fairly good agreement between the analytical and calculated values of c/a . The predicted values for the radius of contact were also in reasonably good agreement with the actual values observed for the tests.

The scanning laser microscope was again used to produce photos of the pads and specimens. The left fretting pad used in test 5 is shown in Figure 3-9. The slip and stick zones are clearly visible in this figure, which is unusual for a test that went to specimen failure. The left side of the specimen used in test 5 is shown in Figure 3-10. This is the specimen discussed earlier where the fracture plane was above the fretting scar on the left side of the specimen.

It is interesting that cracking cannot be observed in Figure 3-10. It seems reasonable that cracking would initiate on both sides of the specimen since both sides are under the same loading conditions. Cracking was observed in the fretting pads of test 2. The cracking in the right fretting pad used in test 2 is shown in Figure 3-11. Cracking can be seen on the left edge of the scar. Cracking was also found on the opposite side of the scar, but it cannot be seen in

Test	a (μm , Pred.)	a (μm , Act.)	c/a (Pred)	c/a (Act.)	Cracking
1 L	195	200	0	*	no
1R	195	241	0	0.34	no
2 L	195	216	0.39	0.47	yes
2 R	195	247	0.39	*	yes
3 L	195	280	0.75	*	no
3 R	195	*	0.75	*	no
5 L	195	195	0.78	0.76	no
5 R	195	230	0.78	*	no
5 L (spec)	195	196	0.78	0.77	no
5 R (spec)	195	175	0.78	*	no
6 L	195	252	0.75	*	no
6 R	195	243	0.75	*	no
7 L	195	252	0.43	*	no
7 R	195	*	0.43	*	no
8 L	164	189	0	*	no
8 R	164	302	0	*	no
9 L	164	233	0.74	0.64	no
9 R	164	197	0.74	0.65	no

Table 3.10: Comparison of the analytical versus actual fretting geometry (Ti-6Al-4V).

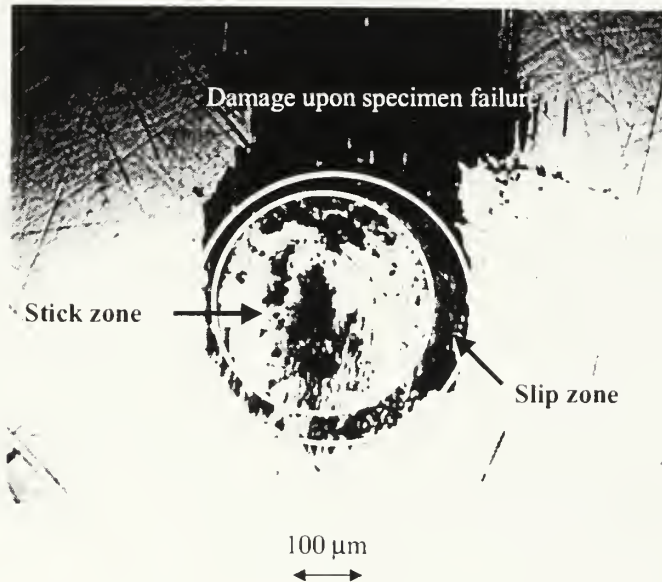


Figure 3-9: Picture of the left fretting pad used for test 5 (Ti-6Al-4V).

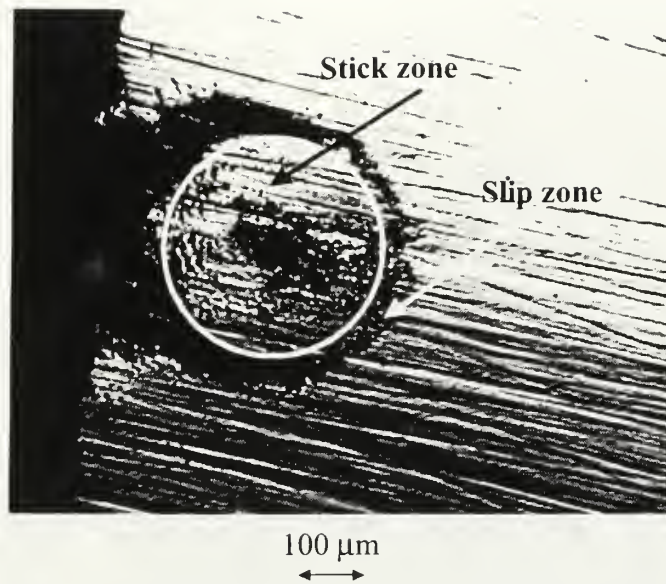


Figure 3-10: Picture of the left side of the specimen used for test 5 (Ti-6Al-4V).

this photo. The crack appears to have begun near the edge of contact; however, the slip and stick zones are not distinguishable and the exact location of crack initiation is not certain.

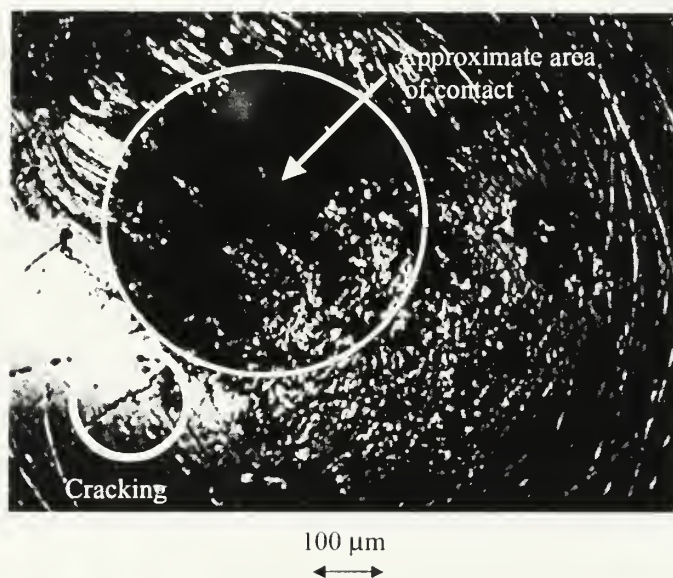


Figure 3-11: Picture of cracking in the right fretting pad used for test 2 (Ti-6Al-4V).

Chapter 4

Fretting Fatigue Life Prediction Analysis

4.1 Introduction

There are two basic approaches used to predict component life for plain fatigue: the *damage tolerant* approach and the *total life* approach. The damage tolerant approach assumes an initial flaw exists in the material and the life of the structure is the number of loading cycles it takes to propagate an initial flaw to a critical length where failure occurs. In this method only crack propagation is considered. The total life approach considers the whole failure crack formation process, from initiation to component failure. This work uses both approaches to analyze the fretting fatigue phenomenon to provide as much insight into the problem as possible.

Developing a life prediction method to be used in fretting fatigue applications is difficult because the effects of fretting are most damaging during the stages of fatigue crack growth which have the least developed methodologies: the crack initiation stage and the short crack propagation stage. Methods do not even exist for plain fatigue to determine the number of cycles required to initiate a crack and propagate it the distance required to use long crack propagation techniques. The varying stress fields introduced by fretting make this task even more difficult.

The deleterious effects of fretting on fatigue were shown in the preceding chapter. The applied bulk stress needed to cause fatigue failure in materials under fretting conditions can

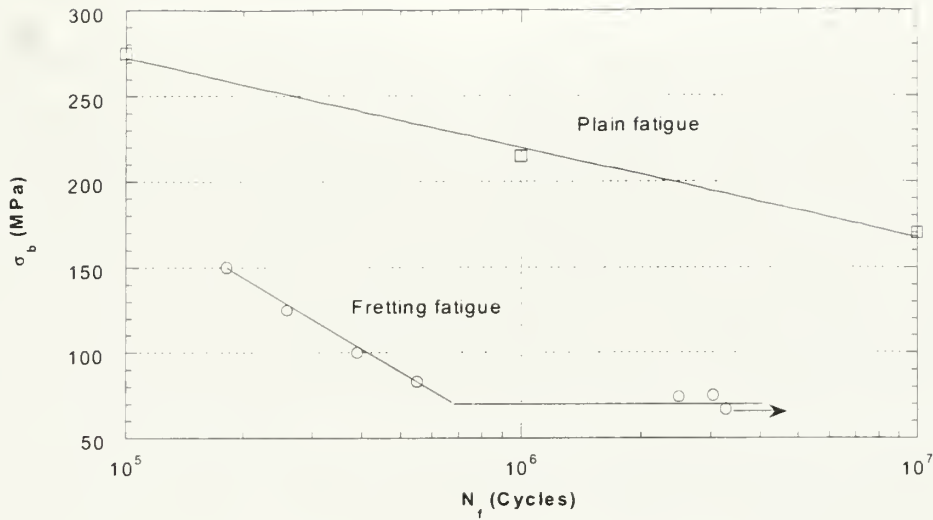


Figure 4-1: Comparison of the S-N curves for plain fatigue and fretting fatigue for Al 7075-T6 ($\sigma_{cc} = 337$ MPa).

be much lower than the endurance strength of the material. The endurance strength of Al 7075-T6 is 176 MPa; however, under fretting conditions failures were observed at bulk stresses as low as 74 MPa. The damaging effects of fretting on fatigue life is shown graphically in Figure 4-1 for Al 7075-T6. The constant contact loading series of tests ($P = 20$ N, $Q = 15$ N) has been used for the fretting fatigue S-N curve shown in the figure. Therefore, the fretting S-N curve represents only one contact loading condition. The curve could change significantly for a different set of contact load parameters. This will be discussed in more detail later in this chapter.

The fretting S-N curve has been shifted down considerably relative to the plain fatigue S-N curve in Figure 4-1. Therefore, cracks are initiating and growing to failure in fretting conditions where there was no failure for the plain fatigue conditions, even at higher alternating stresses, which demonstrates the critical role of fretting in crack initiation. The fretting fatigue curve also exhibits an endurance limit. The existence of an “endurance” type limit for fretting fatigue is discussed in more detail in the following section.

4.2 Total Life Approach

The total life approach is further subdivided into two categories; the stress-life method and the strain-life method. The stress-life method is used in high cycle fatigue (HCF) applications where the applied stresses are maintained in the elastic range. The strain-life method is used for low cycle fatigue (LCF) applications where plastic strains make up a significant portion of the total strains in the material. The fretting fatigue phenomenon is a HCF problem and the stresses calculated in the previous chapter were found to be within the elastic region, so the stress-life method has been chosen for further investigation. The stress-life approach is still widely used in industry today.

The stress-life approach is based upon the work of Wöhler performed in the 1850's and 1860's, who developed the $S - N$ diagram. The $S - N$ diagram is a plot of the alternating stress, S , versus the number of cycles to failure, N . The work of Wöhler clearly showed a relationship between the applied stress amplitude and the number of cycles to failure and indicated an existence of an endurance limit for some materials. The endurance limit is the applied alternating stress below which fatigue failure will not occur. Some materials do not exhibit an endurance limit. For these materials the endurance strength has been defined as the stress amplitude which produces specimen failure at 5×10^6 cycles, or more often shown as $2N = 1 \times 10^7$ reversals.

A mathematical expression for the stress-life relationship found by Wöhler was not produced until 1910 by Basquin [26]. Basquin noted that a linear relation existed between the applied stress amplitude and the number of reversals to failure when plotted on a log-log scale. The relationship is given by:

$$\frac{\Delta\sigma}{2} = \sigma_a = \sigma'_f (2N_f)^b \quad (4.1)$$

where σ_a is the applied stress amplitude, σ'_f is the fatigue strength coefficient, b is the fatigue strength exponent and $2N_f$ is the number of reversals to failure. The fatigue strength coefficient, σ'_f , is approximately equal to the true fracture strength of the material, σ_f . The fatigue strength exponent, b , is generally between -0.05 to -0.12. This equation has been used quite extensively for many years. The values for σ'_f and b are known for many different materials and can be found in many text books, including references [24] and [22].

The Basquin relationship given in Equation 4.1 can be rearranged to give

$$N_f = 0.5 \left(\frac{\sigma_a}{\sigma'_f} \right)^{1/b} . \quad (4.2)$$

A modification to the equation above is proposed for fretted components such that the number of cycles to failure is now given by:

$$N_f = 0.5 \left(\frac{F \sigma_b}{\sigma'_f} \right)^{1/b} \quad (4.3)$$

where F is the fretting correction factor, which is used to account for the premature initiation of cracking in fretted components. To be consistent with earlier notation, σ_b has been substituted in for σ_a . Equation 4.3 is very simple and if its validity can be proved, it would be a valuable design tool. The critical parameter in the modified Basquin expression is the fretting correction factor, F . The values for the fatigue strength exponent, b and the fatigue strength coefficient, σ'_f are taken to be the same as for plain fatigue. They have not been modified to account for fretting. Equation 4.3 can be rearranged such that F is given by:

$$F = \frac{(2N_f)^b \sigma'_f}{\sigma_b} . \quad (4.4)$$

The experimental results given in Table 3.1 have been used to determine F for each test. The analysis of F is separated into two categories; the constant applied bulk stress results and the constant contact stress results. This was done to determine the effect of the contact and bulk stresses on F . F is assumed to be a function only of the bulk and contact stresses. The constant bulk stress results are given in Table 4.1. The values of F for the unfailed specimens were determined using the number of cycles where the tests were stopped; therefore, these values of F are maximum values for the given contact conditions.

Figure 4-2 is a graphical representation of the information displayed in Table 4.1. This figure shows the general trend of the data, as the effective stress due to contact is increased, the fretting correction factor, F , also increases. The plot includes the unfailed specimens in order to display the behavior of F at low contact stresses. The F values for the unfailed

Test	N_f (Cycles)	σ_b (MPa)	σ_{ec} (MPa)	F
1	449,500	83	335	2.820
4	361,000	83	366	2.896
6	530,000	83	309	2.758
7	3,300,000 (No failure)	83	264	2.189
8	10,680,000 (No failure)	83	248	1.860
9	803,000	83	292	2.617
10	2,940,000	83	266	2.223
11	3,450,000 (No failure)	83	264	2.160
12	616,500	83	285	2.706
18	2,608,000 (No failure)	83	280	2.250
19	549,000	83	337	2.746

Table 4.1: The necessary data to determine F and its relationship with the contact stresses.

Test	N_f (Cycles)	σ_b (MPa)	F
19	549,000	83	2.746
28	3,050,000	75	2.449
29	390,000	100	2.379
30	258,063	125	2.001
31	181,118	150	1.748
32	2,497,226	74	2.545
1	449,500	83	2.820

Table 4.2: Fretting correction factors for different bulk stresses, constant contact loads.

specimens are only approximations, however they do represent the maximum value that the fretting correction factor could be for these tests. As can be seen in Figure 4-2, the initial slope of the F curve is fairly flat then rises sharply before trailing off again at the high contact stress values. The initial slope may even be less, because the F values for the unfailed specimens are their maximum values. These values may actually be much lower. It must be stressed that these results are for one value of σ_b , a different bulk loading will yield a different curve.

The values of F for the constant contact loading tests are given in Table 4-3. Only the tests that were cycled to failure were included in this table. Table 4.2 has also included test number one. The contact loading for this test is nearly identical to the others, $P = 20.8$ N versus 20.0 N used in the other tests. The plot of F versus σ_b is displayed in Figure 4-3.

From Figure 4-3, it can be seen that for a given contact stress, F decreases as the bulk loading is increased except for the two low bulk load cases (tests 28 & 32). These two cases will be discussed again later.

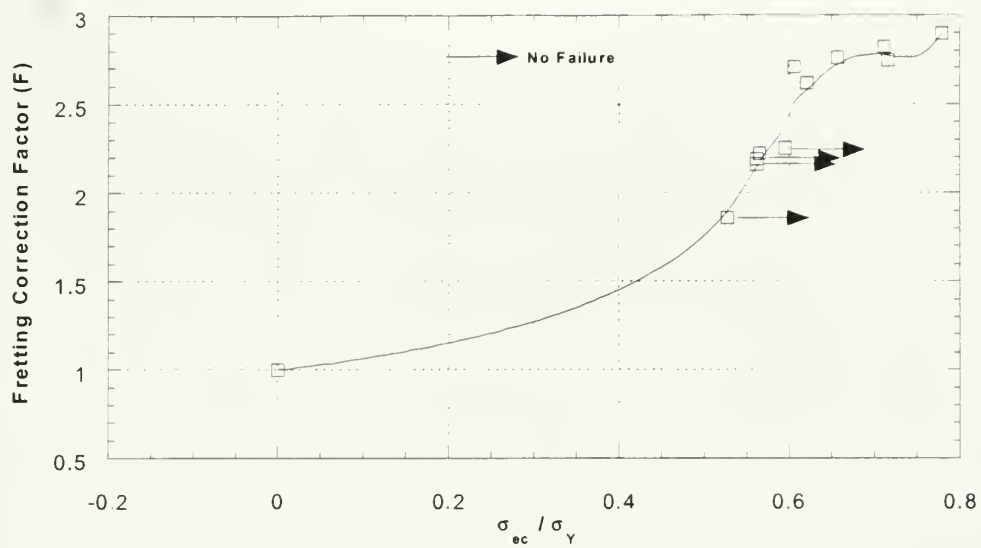


Figure 4-2: Plot of the Fretting Correction Factor, F versus the effective stress due to contact, $\sigma_b = 83$ MPa.

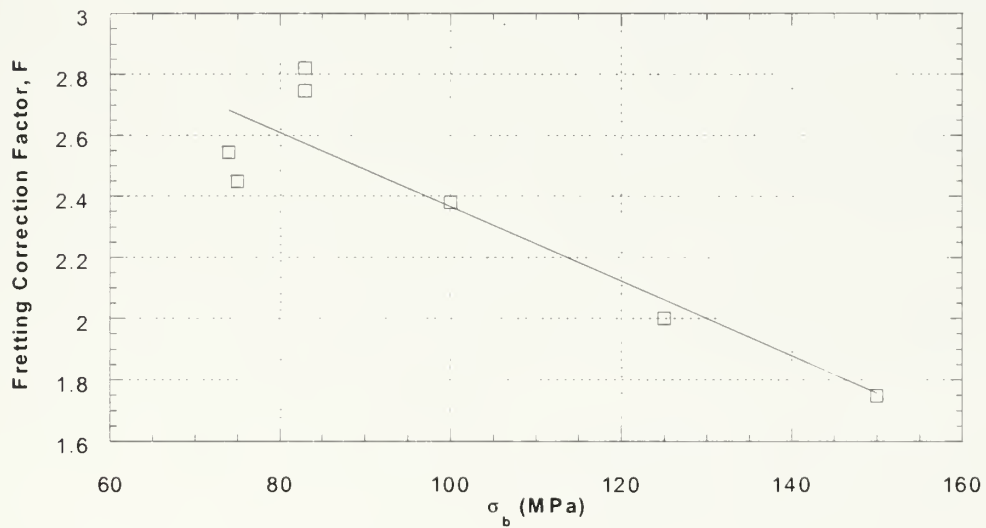


Figure 4-3: Plot of F versus applied bulk stress, while maintaining constant contact loads for Al 7075-T6 ($\sigma_{ec} = 337$ MPa).

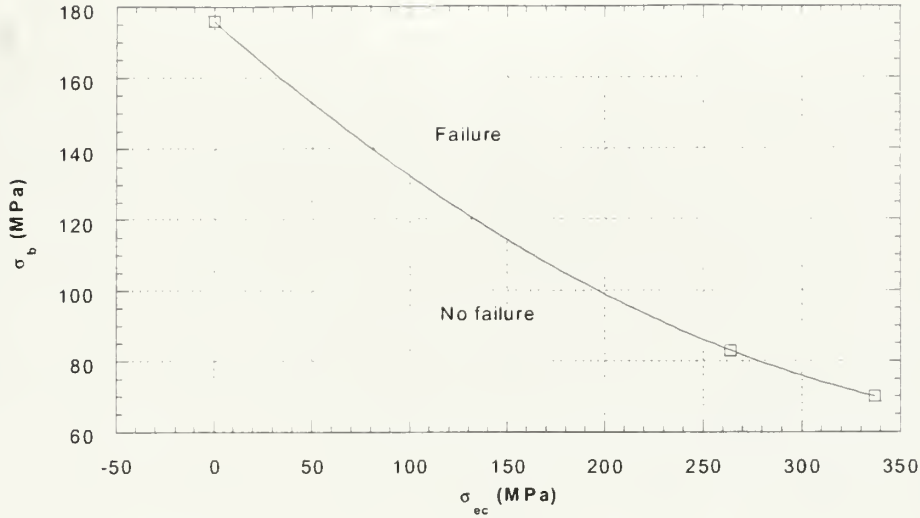


Figure 4-4: Plot of the combination of bulk and contact loading above which fretting fatigue failure will occur for Al 7075-T6.

The constant contact stress analysis and the constant bulk stress analysis will now be combined to provide an estimate of the general behavior of F for various contact and bulk loadings. The knock-down factor idea discussed earlier can aid in this effort. Two thresholds have been found for the two series of tests. Given $\sigma_b = 83$ MPa, specimen failure will not occur if $\sigma_{ec} < 264$ MPa, and given $\sigma_{ec} = 337$ MPa, specimen failure will not occur if $\sigma_b \lesssim 70$ MPa. These two thresholds can be combined with the endurance strength of the material to produce the failure envelope curve shown in Figure 4-4. Specimen failure is predicted for combinations of contact and bulk loadings which fall above the curve.

Figure 4-4 can now be used to analyze Figure 4-2. For $\sigma_{ec} < 264$ MPa fretting will not cause specimen failure if $\sigma_b \leq 83$ MPa; therefore $F = 1.0$ for these loading conditions. Figure 4-2 can now be redrawn as seen in Figure 4-5.

The behavior of the curve in Figure 4-5 is very interesting. Fretting has no effect on the fatigue life of the specimen for a large range of σ_{ec} . However, once the threshold value of σ_{ec} is crossed, the impact on the fretting correction factor, F , is quite significant. Below the threshold, the contact stresses are not high enough to initiate and grow the crack to the length required for long crack propagation by the bulk stress. Once the threshold contact stress is

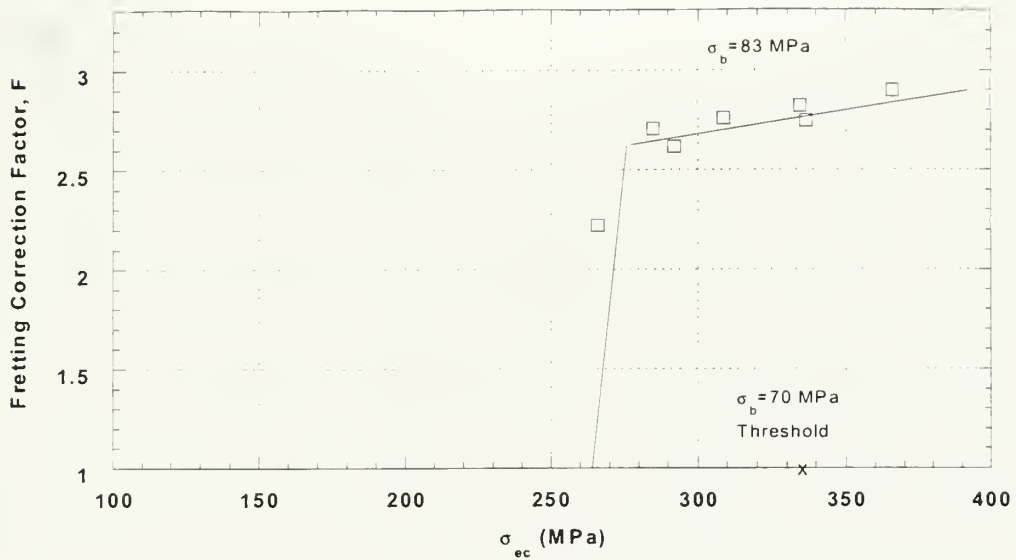


Figure 4-5: Revised plot of F versus σ_{ec} for Al 7075-T6, $\sigma_b = 83$ MPa.

reached cracks will grow enough to be controlled by the bulk stress, but the rate at which this occurs is not greatly effected by how far above the threshold the contact stresses are. The steep portion of the F curve appears to be a very narrow region surrounding the threshold. The slope of the upper portion of the curve is relatively flat.

The constant contact loading data in Table 4.2 and Figure 4-4 can now be used to estimate the behavior of F for other bulk loading conditions as shown in Figure 4-6. The threshold values for $\sigma_b = 100$ MPa and $\sigma_b = 125$ MPa were determined using the failure envelope curve. The shape of the curves were assumed to be similar to that found for $\sigma_b = 83$ MPa. It can be seen that the F curves for the 100 and 125 MPa bulk loading cases pass through the previously determined values of 2.38 and 2.0 at $\sigma_{ec} = 337$ MPa.

Tests 28 & 32 discussed earlier provide results that support the validity of the curves presented above. The F value found for these two cases fell below the curve for the results plotted in Figure 4-3. The threshold σ_{ec} determined from Figure 4-4 is 311 MPa for $\sigma_b = 74$ MPa. Therefore, the contact stress of 337 MPa is approaching the threshold value and could be on the steep portion of the F curve, which would result in an F value lower than the expected

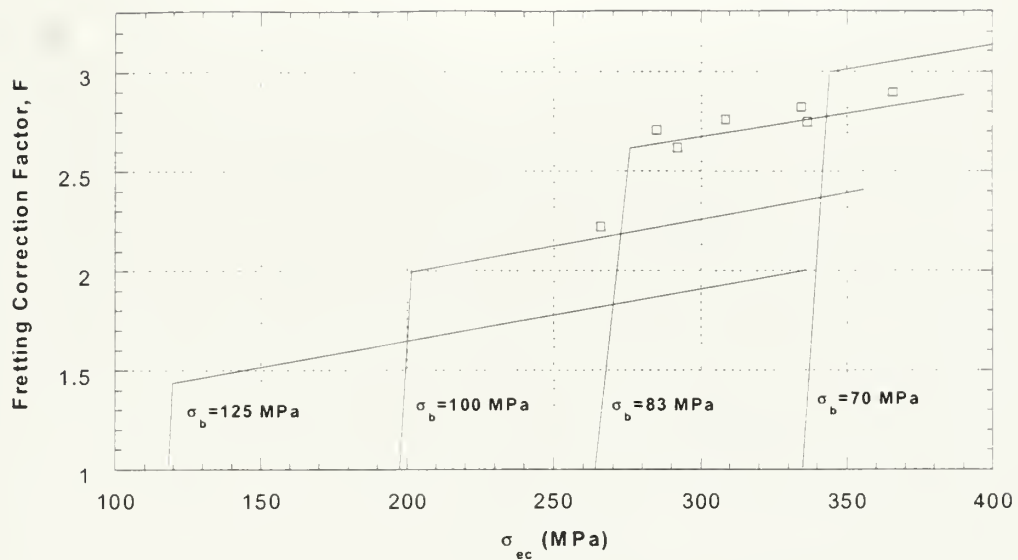


Figure 4-6: Plot of the predicted behavior of F versus σ_{ec} for various bulk loadings (Al 7075-T6).

peak value.

For a given set of loading conditions Figure 4-6 can be used to determine F , which can then be substituted back into equation 4.3 to determine the component life. However, Figure 4-6 is only a rough approximation of the behavior of F for various loading conditions. Many more tests need to be conducted to determine a better estimate for the behavior of F . The threshold contact stress values are the most critical values because it is there where the correction factor is changing significantly and hence where fretting fatigue life is changing the most.

The advantages of this method are that it is simple in form and utilizes the familiar stress-life approach widely used in industry today. However, to implement this method will require considerable experimental work for many different materials. The method also does not provide information on the location of crack initiation. The method uses the contact stresses at the edge of contact, but this is not always the location of crack initiation.

The analysis performed in this section has produced some very interesting results which are:

- A rough approximation for the component failure envelope as a function of the bulk and contact stresses has been determined and is shown in Figure 4-4.

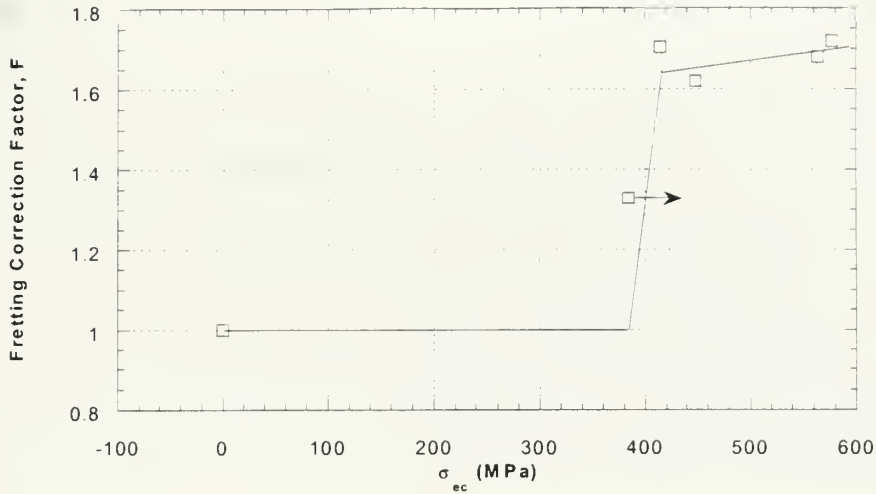


Figure 4-7: Plot of F versus σ_{ec} for Ti-6Al-4V ($\sigma_b \simeq 300$ MPa).

- The slope of the top of the F curve is relatively flat indicating that the fatigue life is not greatly affected by changes in the effective stress due to contact in this region.
- F acts almost as a step function making the determination of the threshold stress values of great importance.

The same analysis was also performed for the Ti-6Al-4V tests recorded in the previous chapter. Tests 5-9 from Table 3.7 were used to determine F as a function of σ_{ec} for $\sigma_b \simeq 300$ MPa. The results are shown in Figure 4-7. This curve is based on limited experimental data, but the same type of behavior as seen with the aluminum alloy seems to be present for the titanium alloy. For the given bulk loading, $F = 1$ until $\sigma_{ec} \simeq 390$ MPa then it quickly jumps to $\simeq 1.7$.

4.3 Damage Tolerant Approach

4.3.1 Al 7075-T6

The second life prediction approach used to analyze the fretting fatigue problem is the damage tolerant approach. Using the experimental results from the preceding chapter, this work

attempts to determine the relative magnitudes of the crack nucleation lifetime and the long crack propagation lifetime. The crack nucleation lifetime used in this work is the life spent initiating and growing the fatigue crack to the length where the fretting stresses are approximately zero. This approach is used by Szolwinski and Farris [30] in their fretting fatigue life prediction method. The long crack propagation life then is only influenced by the bulk stress. Linear elastic fracture mechanics can be used to determine this life. This long crack propagation life can then be compared with the total fatigue life from the experiments to determine the relative magnitudes of the two stages of fatigue life. The approach is demonstrated using the Al 7075-T6 experiments and is applied in the following section to the Ti-6Al-4V experiments.

Paris, Gomez and Anderson [31] in 1961 and Paris and Erdogan[32] in 1963 demonstrated that a power law relationship exists between the crack growth increment da/dN and the stress intensity factor range ΔK . This relationship is given by:

$$\frac{da}{dN} = C(\Delta K)^m \quad (4.5)$$

where C and m are scaling constants, and

$$\Delta K = K_{\max} - K_{\min}, \quad \text{for } K_{\min} > 0$$

$$\Delta K = K_{\max}, \quad \text{for } K_{\min} < 0.$$

Observations were made of the failed test specimens to determine the shape of the propagating crack. It was determined that the cracks could be best characterized as surface elliptical cracks with a ratio of $a/c = 0.9$. A diagram of this geometry is shown in Figure 4-8, with the thickness and width of the fatigue specimens also given.

The stress intensity factor equation for the surface elliptical crack geometry was determined by Newman and Raju [33] in 1981. For a finite plate subjected to a remote uniform tensile stress, S , the stress intensity factor is given by:

$$K_I = S\sqrt{\pi\frac{a}{Q}}F\left(\frac{a}{t}, \frac{a}{c}, \frac{c}{W}, \phi\right) \quad (4.6)$$

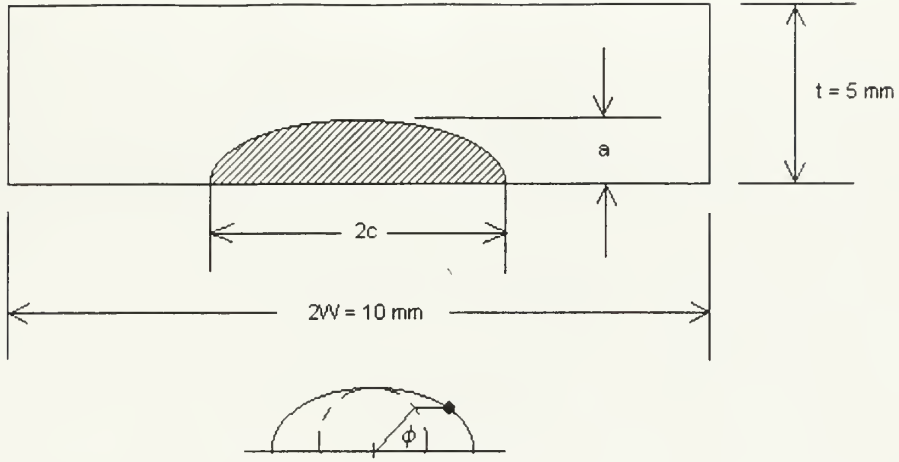


Figure 4-8: Diagram showing the elliptical crack geometry.

where

$$Q = 1 + 1.464 \left(\frac{a}{c} \right)^{1.65} \text{ for } \frac{a}{c} \leq 1.$$

The expression for F was obtained using a systematic curve-fitting procedure [33]. Note this F is not the same F described in the previous section and a in these expressions refers to the crack geometry and not the contact radius. The expression for F is given by:

$$F = \left[M_1 + M_2 \left(\frac{a}{t} \right)^2 + M_3 \left(\frac{a}{t} \right)^4 \right] f_\phi g f_w \quad (4.7)$$

where

$$M_1 = 1.13 - 0.09 \left(\frac{a}{c} \right) \quad (4.8)$$

$$M_2 = -0.54 + \frac{0.89}{0.2 + (a/c)} \quad (4.9)$$

$$M_3 = 0.5 - \frac{1.0}{0.65 + (a/c)} + 14 \left(1.0 - \frac{a}{c} \right)^{24} \quad (4.10)$$

$$g = 1 + \left[0.1 + 0.35 \left(\frac{a}{t} \right)^2 \right] (1 - \sin \phi)^2 \quad (4.11)$$

Parameter	Value
m	4
C	8.6×10^{-12}
a_0	850 μm
a_f	2.5 mm
t	2.5 mm

Table 4.3: Values used in the Paris life calculations for Al 7075-T6. Consistent units for C are meters and MPa.

$$f_\phi = \left[\left(\frac{a}{c} \right)^2 \cos^2 \phi + \sin^2 \phi \right]^{1/4} \quad (4.12)$$

$$f_w = \left[\sec \left(\frac{\pi c}{2b} \sqrt{\frac{a}{t}} \right) \right]^{1/2}. \quad (4.13)$$

The function, f_w is the finite width correction.

The above equations can now be used to find K given any a . The expression for the stress intensity factor is now substituted back into the Paris form, Equation 4.5 and the equation is numerically integrated from an initial crack length a_0 to the critical crack length a_f to find the crack propagation life. Using $\phi = 90^\circ$, the propagation life, N_{fp} is given by:

$$N_{fp} = \frac{1}{C (\Delta\sigma)^4 \pi^2} \int_{a_0}^{a_f} \frac{da}{(0.67)^4 a^2 \left[1.05 + 0.27 \left(\frac{a}{t} \right)^2 - 0.145 \left(\frac{a}{t} \right)^4 \right]^4 \left[\sec \left(\frac{1.11\pi a}{2W} \sqrt{\frac{a}{t}} \right) \right]^4} \quad (4.14)$$

The values used in the propagation life calculations are displayed in Table 4.3 [35]. The value used for a_0 is approximately four times the contact radius for the tests conducted on the aluminum alloy. The stresses due to contact decay away very quickly and are approximately zero at a depth of $1.5a$. However, if $1.5a$ is used for a_0 , the calculated propagation life is greater than the experimental life, which cannot be true. Therefore, a_0 was set equal to $4a$. The value used for a_0 must also be long enough, such that it includes at least a few grain diameters. The average grain size for the Al 7075-T6 specimens was 60 μm [23], so the a_0 used in these calculations encompasses several grain diameters. As can be seen from Table 4.3, only one-half the thickness of the specimen was used in the calculations. This is due to the presence of two cracks in the specimens. When the fracture surfaces of the failed specimens were analyzed, two cracks were observed. One on each side of the fatigue specimen.

Using Equation 4.14, the long crack propagation life was calculated for each test, using σ_b

for $\Delta\sigma$. The stress intensity factor range was also calculated for each test using Equation 4.6, at $a = a_0$, and $S = \sigma_b$ to examine if $\Delta K > \Delta K_0$, the threshold stress intensity factor range at this crack length. The ΔK_0 for Al 7075-T6 at $R = -1$ appears to be approximately $2.3 \text{ MPa}\sqrt{\text{m}}$. This value was determined from a plot in [34]. The plot did not contain $R = -1$ crack growth data; however, using the displayed trends for the other R ratios an estimate for the ΔK_0 for $R = -1$ was made. The calculated values of the propagation life, N_{fp} and the stress intensity factor range at $a = a_0$ for each test are given in Table 4.4.

As can be seen from Table 4.4, the long crack propagation life is a very significant portion of the fretting fatigue life for many of the failed specimens. For these specimens, a very small portion of the life was used to nucleate cracks. The calculated ΔK values in Table 4.4 provide insight into some of the tests where component failure did not occur. It can be seen that for Tests 14-17 and Tests 21-24, $\Delta K < 2.5 \text{ MPa}\sqrt{\text{m}}$ for each of these tests, which is very close to the threshold value for this material.

4.3.2 Ti-6Al-4V

The method used for Al 7075-T6 above is applied to Ti-6Al-4V in this section. The crack geometry for the titanium alloy specimens was very similar to that found above. Again elliptical surface cracks were found; however, cracking was found on only one side of the specimen for this material. The values used to calculate the propagation life for this material are shown in Table 4.5 (a/c corresponds to the elliptic crack geometry). The values used for a_0 are approximately $1.5a$ and $4a$. The first value of $a_0 \simeq 1.5a$, corresponds to the depth at which the tensile stresses due to contact are approximately zero. The second value of $a_0 \simeq 4a$ is used to be consistent with the calculations performed earlier for Al 7075-T6.

The values for m and C were determined using curves found in [37] and [36]. The fatigue crack growth curve in [36] was for solution treated and over-aged (STOA), Bi-modal Ti-6Al-4V, while that found in [37] was for Bi-modal Ti-6Al-4V with no heat treatment. Both curves were made using $R = 0.1$. The values found for C and m for the two cases are shown in Table 4.6. The experimental results displayed in Chapter 3 are for Bi-modal Ti-6Al-4V with no special heat treatment, at $R = -1$. The value of m for this section was set to 5.0, since the applied stress ratio has a small effect on m . The value of C was determined by approximating the

Test	Experimental N_f (Cycles)	N_{fp} (Cycles)	ΔK (MPa \sqrt{m})
1	449,000	408,000	3.17
2	480,000	371,000	3.25
3	395,000	371,000	3.25
4	361,000	408,000	3.17
5	551,000	551,000	2.94
6	530,000	408,000	3.17
7	3,300,000*	408,000	3.17
8	10,680,000*	408,000	3.17
9	803,000	408,000	3.17
10	2,940,000	408,000	3.17
11	3,450,000*	408,000	3.17
12	616,500	408,000	3.17
13	1,410,000*	855,000	2.64
14	2,186,000*	2,280,000	2.06
15	2,500,000*	1,400,000	2.33
16	2,666,000*	1,400,000	2.33
17	2,505,000*	1,400,000	2.33
18	2,608,000*	408,000	3.17
19	549,000	408,000	3.17
20	516,000	807,000	2.68
21	1,540,000*	1,970,000	2.14
22	2,940,000*	1,230,000	2.41
23	1,777,000*	1,600,000	2.26
24	297,000	3,650	10.32
25	135,000	3,650	10.32
26	480,000	6,920	8.79
27	575,000	13,400	7.46
28	3,050,000	612,000	2.87
29	390,000	194,000	3.82
30	258,063	79,300	4.78
31	181,118	38,300	5.74
32	2,497,226	646,000	2.83
33	3,280,000*	961,500	2.56
* No failure			

Table 4.4: Long crack propagation life for Al 7075-T6.

Parameter	Value
a/c	1.0
t	5.0 mm
$2W$	5.0 mm
m	5.0
C	7.0×10^{-14}
a_0	290 μm , 780 μm
a_f	5 mm

Table 4.5: Values used for the propagation life calculations for Ti-6Al-4V.

	STOA, Bi-modal Ti-6Al-4V	Bi-modal Ti-6Al-4V
C	8.13×10^{-14}	1.8×10^{-13}
m	5.12	5.0

Table 4.6: Values of C and m for STOA, Bi-modal Ti-6Al-4V and Bi-modal Ti-6Al-4V (units are meters and MPa).

effect of R on C .

Using the values displayed in Table 4.5, the propagation life was calculated for the nine tests shown in Table 3.7. The propagation lives corresponding to the two different values of a_0 are shown in Table 4.7. As can be seen from the table, the propagation life correlates very well with the actual experimental life of the failed specimens when $a_0 = 1.5a$ is used. Using $a_0 = 1.5a$, the difference in fatigue life for the various tests can be attributed almost entirely to the difference in propagation life. Using $a_0 = 4a$ results in much lower values of N_{fp} . Table 3.7 also displays the calculated ΔK values at $a_0 = 1.5a$. The threshold stress intensity factor range, ΔK_0 , is approximately 3-7 MPa $\sqrt{\text{m}}$ [37].

Test	N_f (Experiment)	$N_{fp}(a_0 = 1.5a)$	$N_{fp}(a_0 = 4.0a)$	ΔK (MPa $\sqrt{\text{m}}, a_0 = 1.5a$)
1	691,612	1,010,000	134,000	4.79
2	109,574	56,800	7,540	8.51
3	107,879	61,200	8,130	8.38
4	31,540 (interrupted)	100,000	13,300	7.60
5	304,456	247,000	32,900	6.34
6	474,656	239,000	31,800	6.38
7	143,683	156,000	20,700	6.96
8	258,576	239,000	31,800	6.38
9	3,257,000(no failure)	239,000	31,800	6.38

Table 4.7: Ti-6Al-4V long crack propagation life.

Chapter 5

Palliatives

5.1 Introduction

The work performed in the previous chapters provide the necessary background for a discussion of fretting fatigue palliatives. The methods developed earlier provide the criteria that can be used to determine how and why certain palliatives work while others do not.

This work will focus on two fretting fatigue palliatives: shot peening and coatings. Both have been shown to be beneficial in increasing fretting fatigue life. Chivers and Gordelier [41] provide a detailed study of several possible palliatives including shot peening and coatings.

5.2 Shot Peening

Shot peening has been used for many years as a way to improve the fatigue properties of components in plain fatigue. The benefits of shot peening were found quite by accident by the Buick Motor Division of General Motors Corporation in the late 1920's [42]. It was found that valve springs that had been blasted with grit to remove scale had greatly improved fatigue properties. It was first thought that the benefits derived from shot peening were due to the work hardening of the surface. However, it was soon discovered that the benefits were caused by the residual stresses introduced at the surface due to shot peening.

In the shot peening process, relatively hard particles are shot against the metal being treated. The particles are generally spherical in shape and are given enough velocity such that the surface

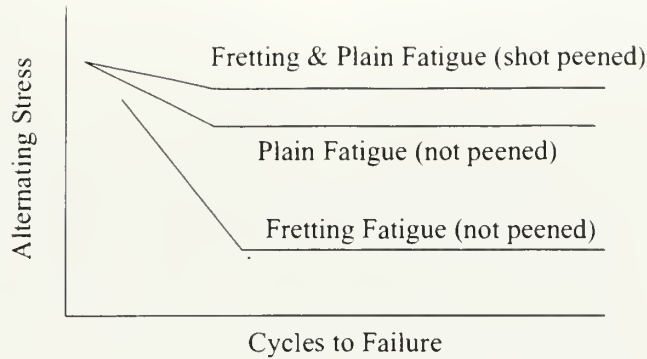


Figure 5-1: Plot showing approximate relationship between shot peened and unpeened specimens for plain and fretting fatigue.

of the metal is indented during impact. The indentations occur due to local plastic yielding and as the surface material attempts to expand, it is restrained by surrounding material below the surface which was not deformed plastically. This restraint of the plastically deformed surface layer causes it to be compressively strained and is residually stressed in compression.

There have been numerous studies conducted showing the benefits of shot peening for plain fatigue conditions. Shot peening has also been demonstrated to be effective in fretting fatigue conditions as well, which is discussed in [38], [39] and [41]. In many materials, shot peening has been shown to increase the fatigue strength such that the fretting fatigue strength is approximately the same as the plain fatigue strength. A simple plot displaying the typical relationship between shot peened and unpeened specimens for fretting and plain fatigue is shown in Figure 5-1. This figure is based upon the work of Bignonnet [39], which studied the effects of shot peening on fretting fatigue. However, this figure is not true for all materials. It is only meant to display the benefits typically observed in shot peened materials.

As discussed earlier, the benefits of shot peening are derived from the residual compressive stresses introduced into the material during the process. The maximum value of the residual compressive stress, often called the magnitude, is not affected by the shot peening process as long as the shot used is at least as hard or harder than the material being treated [43]. The magnitude of the residual compressive stress is material dependent, but has a value of at least one-half the yield strength for that material [43]. The depth of the compressive layer is the

other important parameter in shot peening. The depth of the compressive layer is a function of the hardness and ductility of the peened material, the state of strain in the material when the peening was performed and the characteristics of the shot and shot stream [42]. A typical residual stress profile due to shot peening and the residual stress profile used in this analysis are shown in Figure 5-2. The residual stress profile used in this analysis assumes a flat maximum compressive stress, which goes directly to zero at a given depth. The assumed residual stress profile should actually have a tensile region to balance the residual compressive stresses to satisfy equilibrium. This is shown in Figure 5-3, where σ_{rc} is the residual compressive stress and σ_{rt} is the residual tensile stress required for equilibrium. For equilibrium to be satisfied area $A1$ must equal area $A2$. Therefore the area balance is given by:

$$(pd)(\sigma_{rc}) = (t - pd)(\sigma_{rt}), \quad (5.1)$$

and the ratio of the residual stresses is given by:

$$\frac{\sigma_{rt}}{\sigma_{rc}} = \frac{pd}{(t - pd)}. \quad (5.2)$$

If $(t - pd) \gg (pd)$ then $\sigma_{rt} \rightarrow 0$. It is assumed in this work that $(t - pd) \gg (pd)$, therefore the residual tensile stress has been neglected. Note that the actual maximum compressive stress occurs at some depth below the surface. The actual depth of residual compressive stresses for various materials is given in [43] as well as some residual stress profiles.

The benefits derived from shot peening can also become detrimental to the material if the residual compressive stresses are somehow relieved. The process which caused the residual stresses to be induced into the material also damages the surface of the material and may even introduce microcracks. These microcracks could drastically reduce fatigue life if the residual compressive stresses are relieved. This has been shown to be the case in both plain fatigue and fretting fatigue. Gray, Wagner and Lütjering [44] show the detrimental effects on plain fatigue life of shot peening when the residual compressive stresses are thermally relieved. The fatigue strength of the material is significantly reduced for the shot peened, stress relieved specimens as compared to the original electrolytically polished specimens. Figure 5-4, from [44], demonstrates this effect. In Figure 5-4, SP is shot peened, EP is electrolytically polished

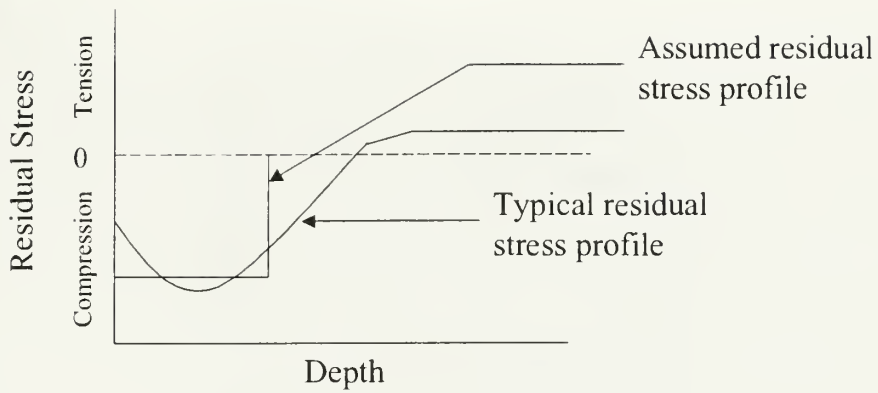


Figure 5-2: Typical stress profile after shot peening and the assumed stress profile used in this work.

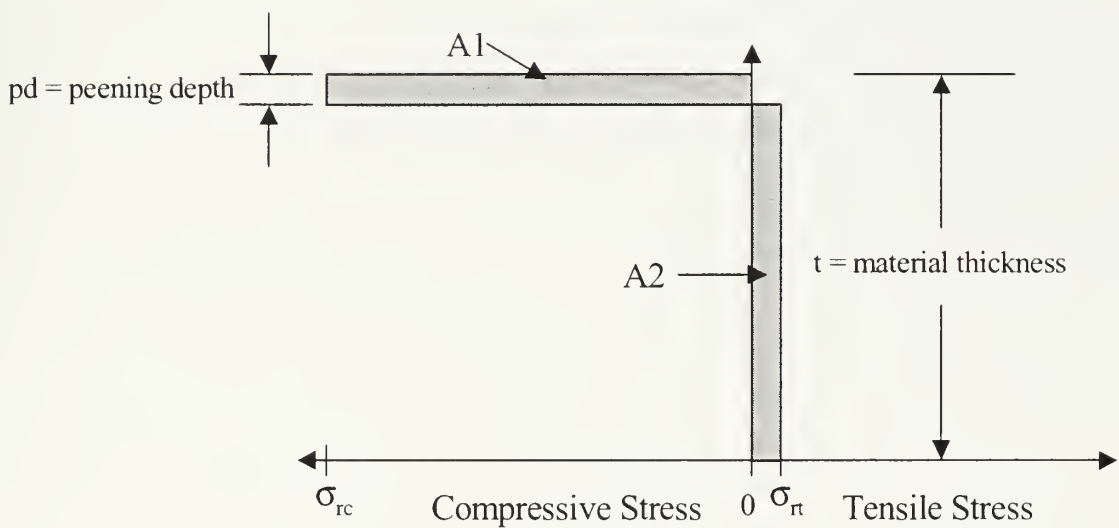


Figure 5-3: Residual stress equilibrium diagram.

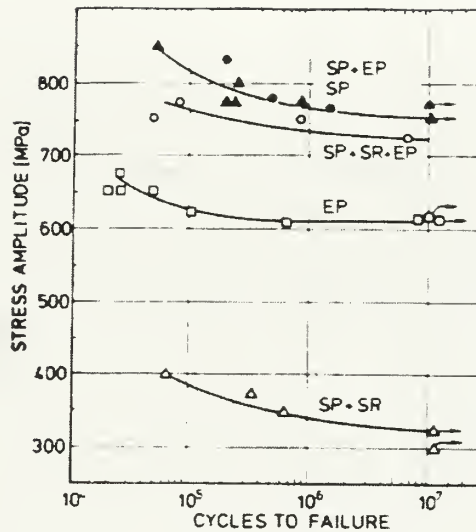


Figure 5-4: Diagram showing the detrimental effects of shot peening if the residual stresses are relieved [44].

and SR is stress relieved. From this figure it can be seen that the fatigue strength for the shot peened and stress relieved specimens is about one-half that of the electrolytically polished specimens at 1×10^7 cycles, the reduction in fatigue strength is quite significant and certainly cannot be ignored. The shot peened and stress relieved curve shifts down relative to the electrolytically polished specimen curve indicating that the difference between the two curves is in the crack initiation stage, just as was found for fretting. The material used in [44] was Ti-6Al-4V with a fine lamellar microstructure and the temperature was 20 °C for this set of test results. The residual stresses were relieved thermally using a heat treatment of 600 °C for one hour. These results were for plain fatigue experiments. Bignonnet [39] displays similar results for fretted specimens. The fretting fatigue strength of the shot peened, stress relieved specimens was similar to that of the unpeened specimens. Waterhouse [38] found similar results in his experimental work. These works demonstrate the importance of the compressive residual stresses and the importance of not allowing them to be relieved.

Laser shot peening does not have the shortcomings discussed above for the typical shot peening process. In the laser shot peening process the surface is unchanged by the peening

process. Shock waves are introduced into the material that are capable of plastically yielding the material and producing compressive residual stresses.

The residual stresses can be relieved either mechanically or thermally. The approximate temperature at which the residual compressive stresses begin to dissipate for various materials can be found in [43]. The residual stresses are relieved mechanically if the total stresses in the material exceed the dynamic elastic limit of the material. The total compressive stress is made up of the shot peening residual stress and the stress due to external loading. The residual stress is relieved by the amount that the total compressive stress exceeds the dynamic elastic limit of the material.

The objective of this section is find the optimum peening depth for various fretting fatigue loading conditions. The magnitude of the residual compressive stresses are fixed by the material, therefore the designer has no control over this aspect of the shot peening process. However, the depth of residual stress can be influenced by variations in peening parameters as shown in [43]. Therefore, the depth of peening becomes the variable design parameter that can be optimized by the designers.

5.2.1 Material Yielding Analysis

A systematic analysis of the shot peening process applied to the sphere on flat surface contact geometry has been conducted in this work. The material used for this analysis is Ti-6Al-4V. The pertinent material properties for Ti-6Al-4V are listed in Table 3.6. The first task was to find the conditions when the residual compressive stresses would begin to be relieved. According to [43], the compressive stresses begin to dissipate thermally at 480 C for Ti-6Al-4V. Mechanical stress relieving begins to occur when the material stresses exceeds the elastic limit of the material. The stress fields for a sphere fretting against a flat surface have already been discussed in Chapter 2 of this work. The surface stresses for this geometry for Al7075-T6 are displayed in Figure 2-2. The stress profile for Ti-6Al-4V is almost identical, the magnitudes are different, but the shape of the curves are the same.

The analysis performed in this chapter assumes the onset of global sliding. This condition provides the highest stresses possible for a given contact loading. If global sliding is assumed, the normal load, P , becomes the critical contact parameter since the tangential load, Q , will

always be equal to μP . The loading which causes the total effective stress, σ_{tot} , to become equal to the yield strength is when material yielding is assumed to occur and is shown in Figure 5-5. The data used to make this figure were determined using a MATLAB script file. A MATLAB routine was written which first scans the surface of the material, then incrementally scans below the contact surface calculating the stresses at each increment, producing a matrix of stresses. The surface is scanned along the $y = 0$ line, where maximum material stresses are. The increment used in the x-direction is $0.02a$. The increment in the z-direction is $0.025a$. The program then finds the maximum effective stress from the matrix of stresses determined during the scan. The stresses at the contact edges are calculated separately. The maximum stress is then compared to the yield stress. If the maximum effective stress is less than the yield stress, the contact loading is increased and the stress calculations are performed again. The process is continued until the contact loading which produces yielding is determined. This was done for five different coefficients of friction and eight different bulk stress conditions. The stresses at the edge of contact are calculated separately because the stresses are indeterminate at the contact origin ($x = y = z = 0$) and the origin would be included in the surface scan if both contact edges are also included. The program used for this analysis is shown in Appendix A.

In Figure 5-5 the yielding curves have been plotted, which show for a given bulk stress, σ_b and a given coefficient of friction, μ , the minimum contact pressure, P_0 , that is needed to cause the total effective stress to exceed the yield stress of the material. For example if $\mu = 0.7$ and $\sigma_b = 0.1\sigma_Y$ then the maximum contact pressure which produces yielding is $\simeq 0.28\sigma_Y$. This example is shown in Figure 5-5. The maximum contact pressure is normalized by the yield strength of the material in this plot. A residual stress of $-0.85\sigma_Y$ is used for this study. This value for the residual compressive stress was determined using an actual shot peening stress profile from [44] and a graph of maximum compressive residual stress versus tensile strength in [43].

As can be seen in Figure 5-5, the contact loading which causes material yielding increases as the applied bulk stress increases until $\sigma_b = 0.4\sigma_Y$. The leading edge of contact, where the compressive stresses due to contact are very high, is the location of yielding for applied bulk stresses less than one-half the yield strength. The location of yielding shifts to the trailing

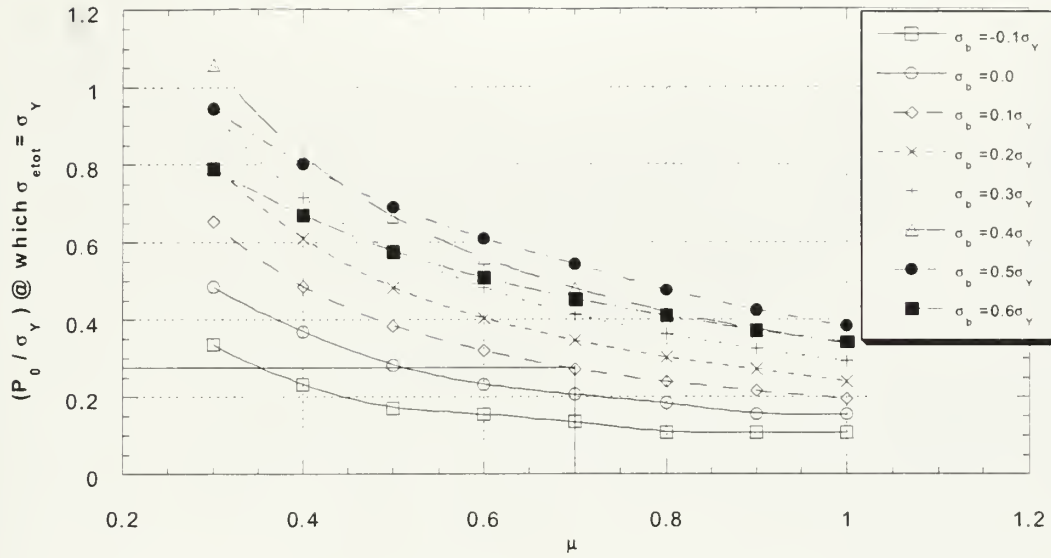


Figure 5-5: The combination of contact and bulk loading which causes the total effective stress to equal the yield stress plotted versus the coefficient of friction.

edge, where the tensile stresses due to contact are very high, when $\sigma_b \geq 0.5\sigma_Y$. Therefore, yielding is controlled by the compressive stresses until the applied bulk stress reaches a value of one-half the yield strength. This explains why the maximum contact pressure which causes yielding actually increases with increasing bulk stress when $\sigma_b < 0.4\sigma_Y$. Figure 5-5 also shows the effect of friction. As the coefficient of friction increases, the contact pressure needed to cause yielding decreases. It can also be seen that the contact loads needed to cause yielding are relatively low for the coefficient of friction typical for Ti-6Al-4V (0.4-0.5); therefore, residual stress relieving due to yielding cannot be ignored. Yielding first occurs at the surface for $\mu > 0.3$. Since yielding usually occurs first at the surface, the depth of yielding must also be found.

5.2.2 Depth of Yielding

The depth of yielding must be found to determine to what depth the residual stresses are being relieved. The von Mises effective stress is again used to determine the yield conditions, i.e. when $\sigma_{\epsilon_{tot}} \geq \sigma_Y$ the material is considered to have yielded. A MATLAB routine was also written to perform this task. The routine used to perform this task is similar to the previous

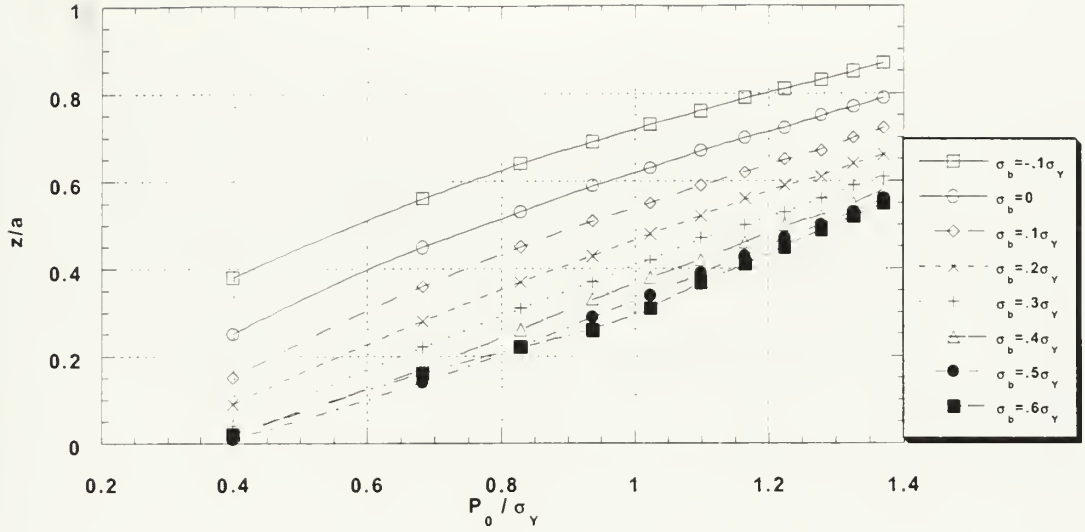


Figure 5-6: Plot of yielding depth, z versus maximum contact pressure for various bulk loadings ($\mu = 1.0$).

one. Again the surface is scanned using an increment of $0.02a$ in the x -direction with $y = 0$ for all points. The stresses are then determined below the surface using an increment of $0.02a$ in the z -direction, which results in a matrix of stresses. The stresses at the edge of the contact are not calculated separately in this routine because the stress profile is much smoother at the edges below the contact surface as shown in Figure 2-3. The depth of maximum stress is found and this depth became the starting point for the iteration to find the depth of yielding. The depth of maximum stress is always the surface for $\mu > 0.3$. The scanning process begins again at the depth just determined using a reduced increment in the z -direction of $0.01a$. The depth is increased until the effective stress is no longer greater than the yield strength of the material. Figure 5-6 displays the results of this analysis for $\mu = 1.0$. The depth, z is normalized by the radius of contact, a , the maximum contact pressure, P_0 , is normalized by the yield strength of the material, σ_Y . Again the residual stress used in this analysis was $\sigma_{residual} = -0.85\sigma_Y$. The MATLAB script file used in this section is shown in Appendix B.

The results displayed in Figure 5-6 follow the expected trends, the depth of yielding increases as the contact load is increased and decreases as the bulk loading is increased until $\sigma_b \simeq 0.5\sigma_Y$.

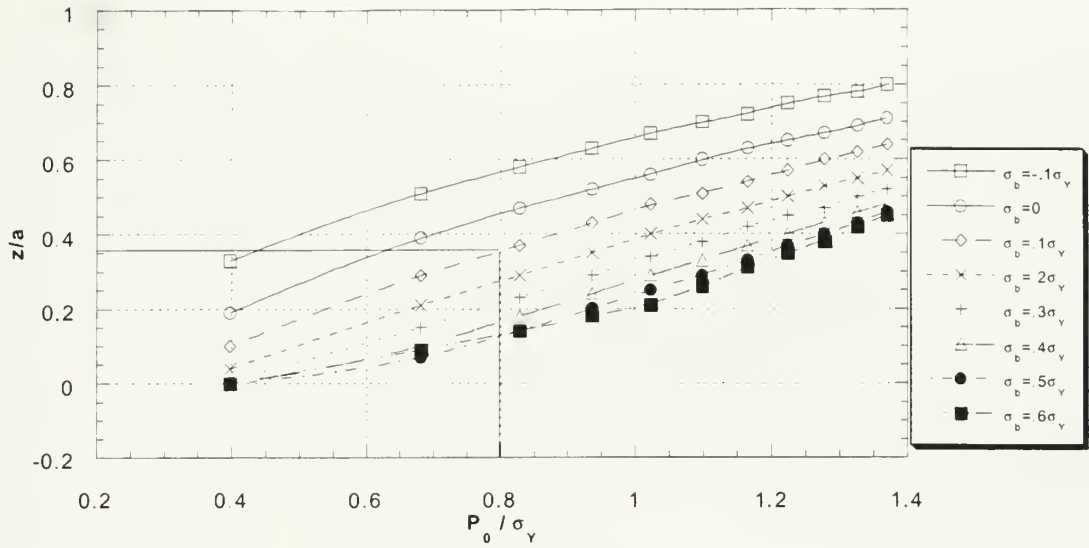


Figure 5-7: Depth of yielding versus maximum contact pressure for various bulk stresses ($\mu = 0.8$).

The depth of yielding decreases with increasing bulk stress due to the large residual compressive stress assumed in the analysis. This same analysis was repeated for three more coefficients of friction, $\mu = 0.8$, $\mu = 0.5$ and $\mu = 0.3$. The results for the three other coefficients of friction are shown in Figures 5-7, 5-8 and 5-9 respectively. As can be seen in these figures, the depth of yielding is reduced significantly as the coefficient of friction is lowered, which again points to the possible benefits of coatings in fretting situations. When the coefficient of friction is reduced to 0.3, there is very little yielding even at very high contact loadings for $\sigma_b \geq 0.4$.

The depth of yielding curves developed in this section can be very useful for design, specifically in the material treatment stage of design. Designers could use these plots with the known contact and bulk loadings and the coefficient of friction and very quickly determine the minimum depth of shot peening to ensure that the compressive residual stresses are not mechanically relieved. For example, if $\mu = 0.8$, $P_0/\sigma_y = 0.8$, and $\sigma_b = 0.1\sigma_y$, the depth of yielding, $z/a \simeq 0.35$. Therefore, the minimum depth of shot peening to avoid mechanical relieving of the residual stresses is $z/a > 0.35$. This example is shown in Figure 5-7. The depth of yielding curves provide important design information, but they only provide part of

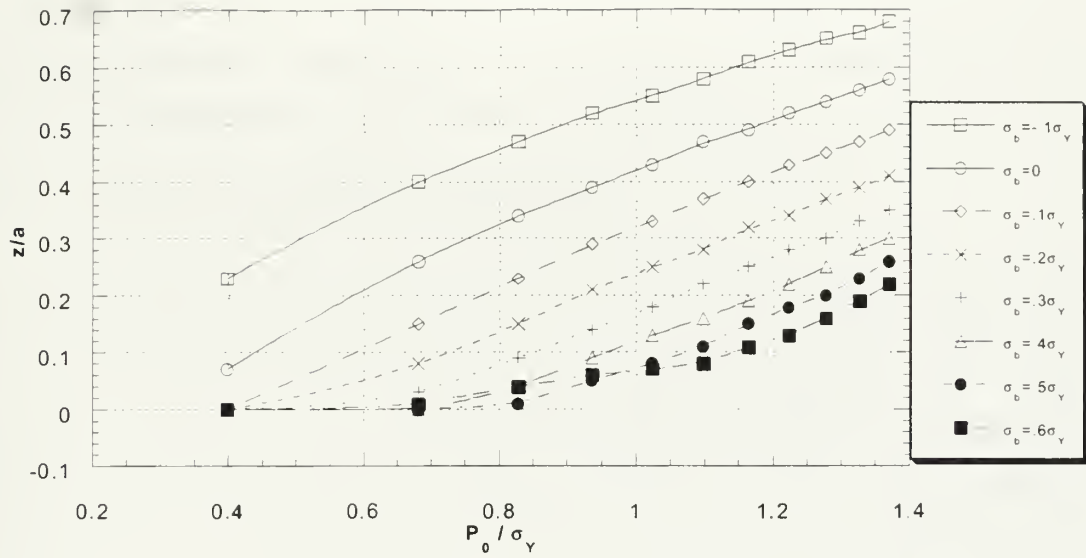


Figure 5-8: Depth of yielding versus maximum contact pressure for various bulk stress loadings ($\mu = 0.5$)

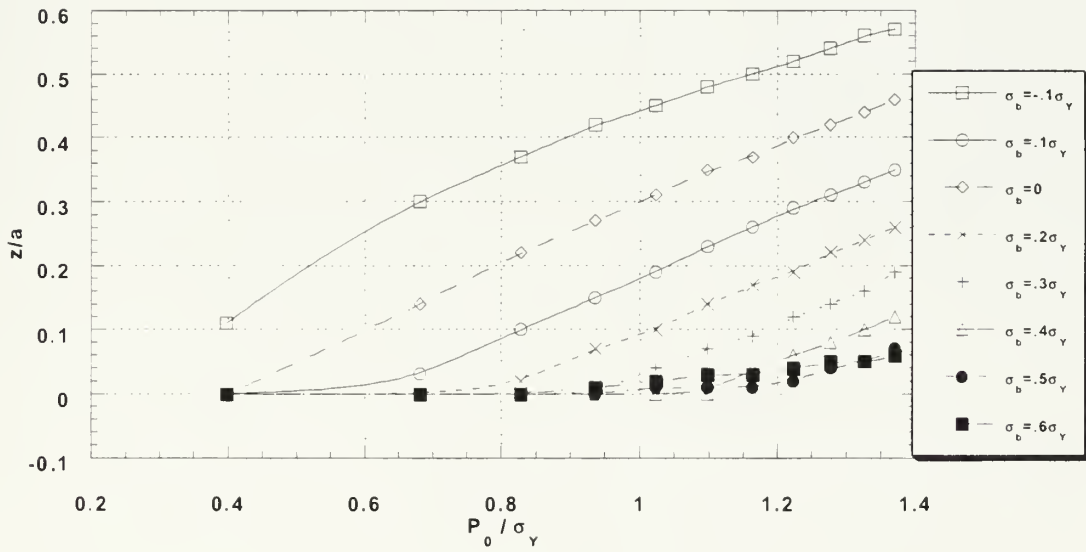


Figure 5-9: Depth of yielding versus maximum contact pressure for various bulk stress loadings ($\mu = 0.3$)

the information needed to determine the optimum shot peening depth. These curves provide the minimum shot peening depth to avoid residual stress relieving but they do not provide information pertaining to the tensile stresses at the crack tip. An additional analysis is needed to provide this information, which is discussed in the next section.

5.2.3 Maximum Principal Stress Analysis

The predicted success of shot peening is based upon two basic assumptions. First, a crack will not propagate unless a tensile stress forces it open near the tip [43]. The second assumption is that a crack tip will not open while a compressive force is acting upon it [43]. These assumptions provide the criteria that is used to determine the optimum shot peening depth. Using the two assumptions stated above, the depth of peening to prevent crack propagation should be the depth at which the maximum principal stress, $\sigma_1 \leq 0$. Therefore, inside this layer of material affected by shot peening, no region of tensile stresses will exist. This does not mean that the entire depth of the material will have no tensile stresses. This only applies in the shot peened region, but that is enough to stop the crack from propagating.

A MATLAB program similar to the two discussed above was written and is shown in Appendix C. The surface is scanned along the x-direction determining the stresses at each point using an increment in the x-direction of $0.02a$, again $y = 0$ for all points. At each point the maximum principal stress, σ_1 , is determined creating a vector of maximum principal stresses. The maximum of this vector is then found and compared to zero. If the maximum of the vector is greater than zero, then the depth is increased by $0.01a$ and the process continued until the maximum principal is less than or equal to zero. This depth then became the required shot peening depth. The shot peening depth, z , which produced a maximum principal stress less than or equal to zero was found for many different loading conditions. Just as in the yielding depth curves, the depth is plotted versus maximum contact pressure for several different values of applied bulk stress. Figure 5-10 displays the depth z , at which $\sigma_1 \leq 0$, for $\mu = 1.0$. Again the depth has been normalized by the contact radius, a and the maximum contact pressure, P_0 , is normalized by the yield strength of the material. This analysis was repeated for three other coefficients of friction, $\mu = 0.8$, $\mu = 0.5$ and $\mu = 0.3$. The curves for $\mu = 0.8$ and $\mu = 0.5$ are shown in Figures 5-11 and 5-12 respectively. The curves for $\mu = 0.3$ are not displayed

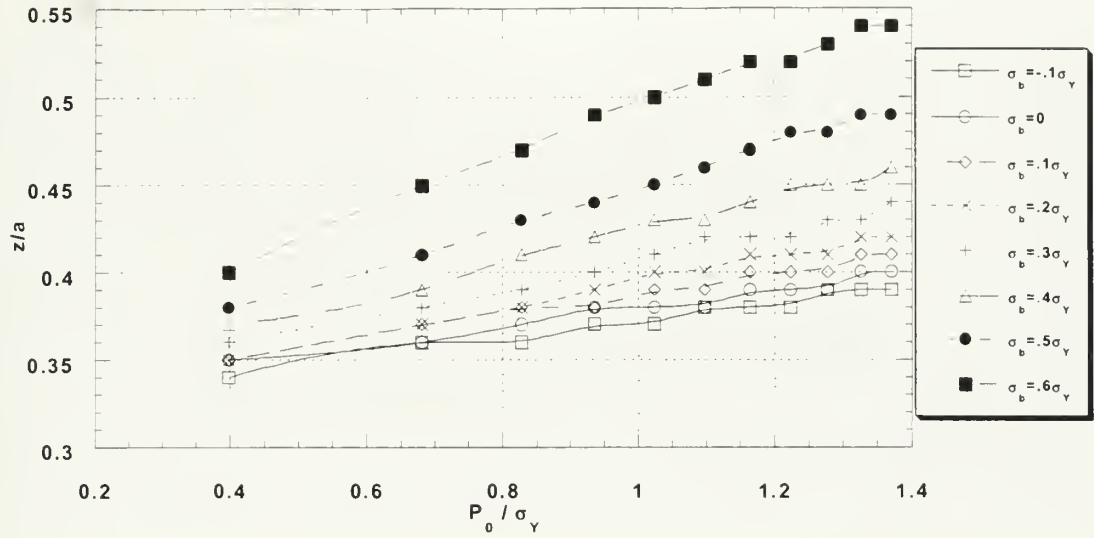


Figure 5-10: The depth at which the maximum principle stress is less than or equal to zero plotted versus maximum contact pressure, for magnitudes of bulk stress ($\mu = 1.0$).

because the required peening depth was less than for $0.10a$ for even the highest load conditions analyzed. The plots again show the advantages of lowering the coefficient of friction. There is a significant reduction in z/a as the coefficient of friction is reduced. As expected the required shot peening depth increases as the applied bulk stress, σ_b is increased. As seen in the figures, the increase in peening depth with increasing σ_b becomes quite significant when $\sigma_b > 0.4\sigma_Y$.

The plots generated in this section cannot be used in isolation, they must be integrated with the plots from the previous two sections of this analysis. Together, these sections provide the designer the information necessary to determine the optimal shot peening depth for the given loading and material conditions.

5.2.4 Integrated Yielding and Maximum Principal Stress Analysis (Optimum Shot Peening Depth)

The depths determined from the two preceding sections provide two different threshold values. The depths output from the material yielding analysis provide the minimum depth to which the specimen must be peened to prevent mechanical relieving of the residual compres-

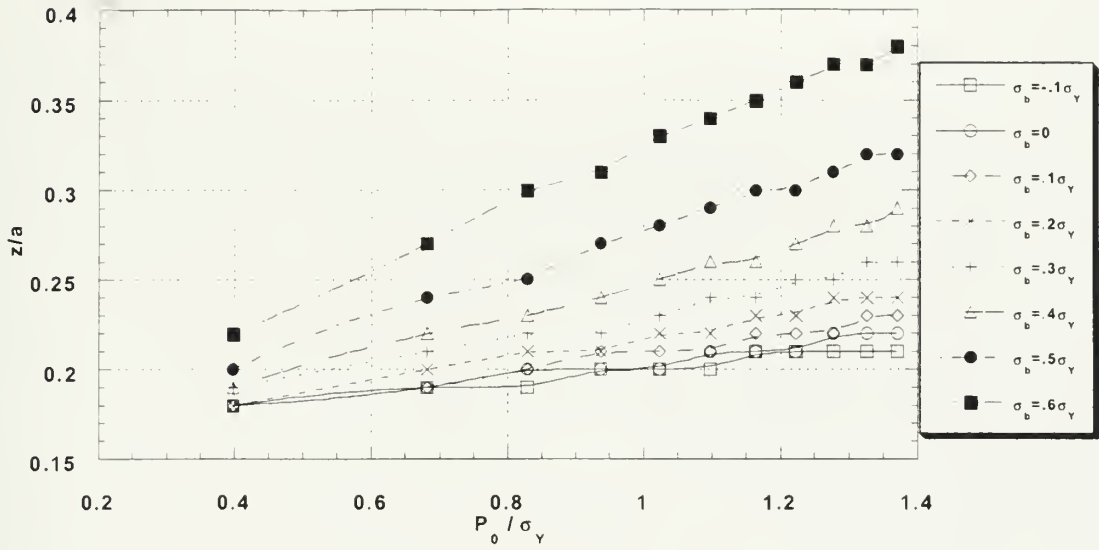


Figure 5-11: The depth at which the maximum principal stress is less than or equal to zero plotted versus maximum contact pressure for various magnitudes of bulk stress ($\mu = 0.8$).

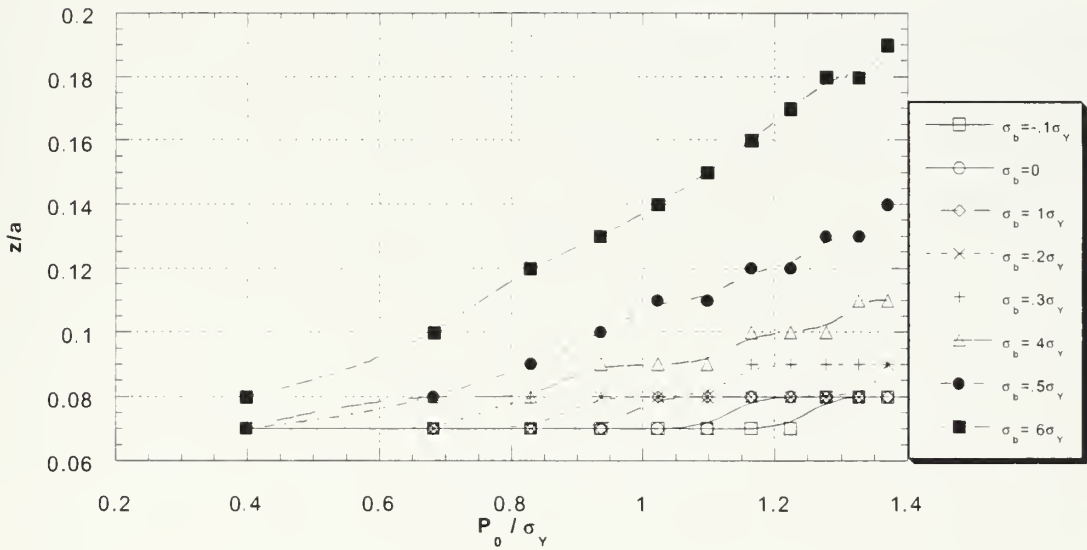


Figure 5-12: The depth at which the maximum principal stress is less than or equal to zero plotted versus the maximum contact pressure for various magnitudes of bulk stress ($\mu = 0.5$).

sive stresses. The depth of yielding analysis determines the minimum peening depth to ensure that the residual compressive stresses remain in the material. The maximum principal stress analysis assumes the residual compressive stresses are still present and determines the peening depth required to prevent crack growth. Therefore, the depth of yielding analysis provides a minimum shot peening depth, but does not provide all information necessary to determine the optimal peening depth. The remaining information is provided by the maximum principal stress analysis, which determines the peening depths at which $\sigma_1 \leq 0$. This analysis assumes the crack will not grow in a region of pure compressive stresses. The two analysis must be combined to form the complete picture, which has been done in Figure 5-13 for $\mu = 1.0$ and $\sigma_b = 0.4\sigma_Y$. As can be seen from Figure 5-13 the limiting curve depends upon the contact loading, a cross-over point occurs at $(P_0/\sigma_Y) \simeq 1.15$. If $(P_0/\sigma_Y) \lesssim 1.15$ the maximum principal stress analysis is the limiting case and controls the optimum peening depth, however if $(P_0/\sigma_Y) \gtrsim 1.15$ the depth of yielding analysis becomes limiting and determines the required peening depth. This example shows the importance of examining both criteria. An example on how to use the figure is also displayed in Figure 5-13. If $(P_0/\sigma_Y) = 0.8$ then the optimum peening depth, $z/a \simeq 0.4$. The designer may choose to shot peen to a slightly greater depth to ensure no tensile stresses exist in the material at that depth.

A second example is given in Figure 5-14 for $\mu = 0.8$ and $\sigma_b = 0.1\sigma_Y$. As can be seen in this figure, the intersection between the two curves occurs at a much lower contact pressure than in the previous example. Contrary to the previous example, the depth of yielding is the limiting curve over most of the contact loading space for the given μ and σ_b . These curves can be generated quite easily from the figures provided in the previous two sections for many other combinations of μ and σ_b , however only two examples will be displayed in this work. In Figure 5-14 the optimum peening depth, z/a , was again found for a contact load of $(P_0/\sigma_Y) = 0.8$. In this example the optimum peening depth was found to be: $z/a \simeq 0.36$. The shot peening depth found in this example would be the minimum recommended because material yielding is still occurring at this depth. The material is just at the yield point, but it is recommended that the material be shot peened to a slightly greater depth to ensure no material yielding and hence, no mechanical residual stress relieving will occur.

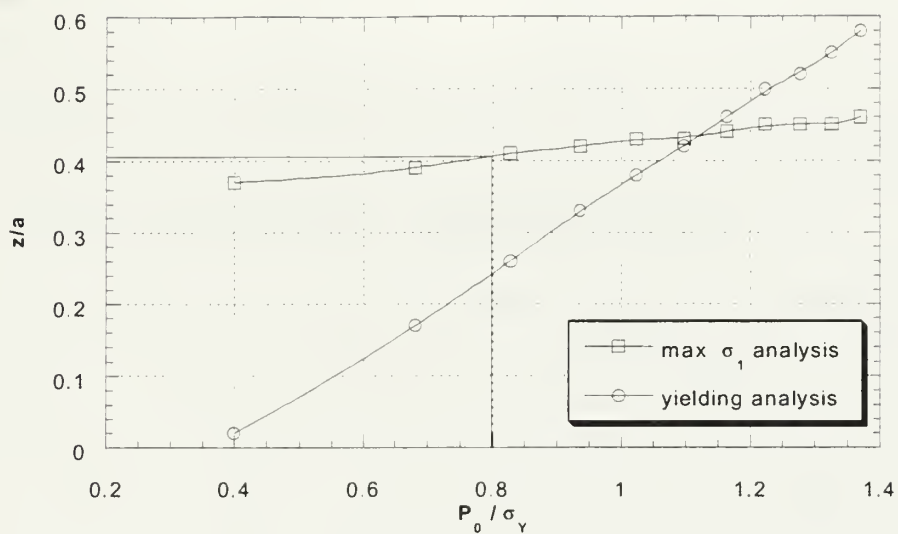


Figure 5-13: Optimum peening depth plotted versus maximum contact pressure for $\mu = 1.0$ and $\sigma_b = 0.4\sigma_Y$.

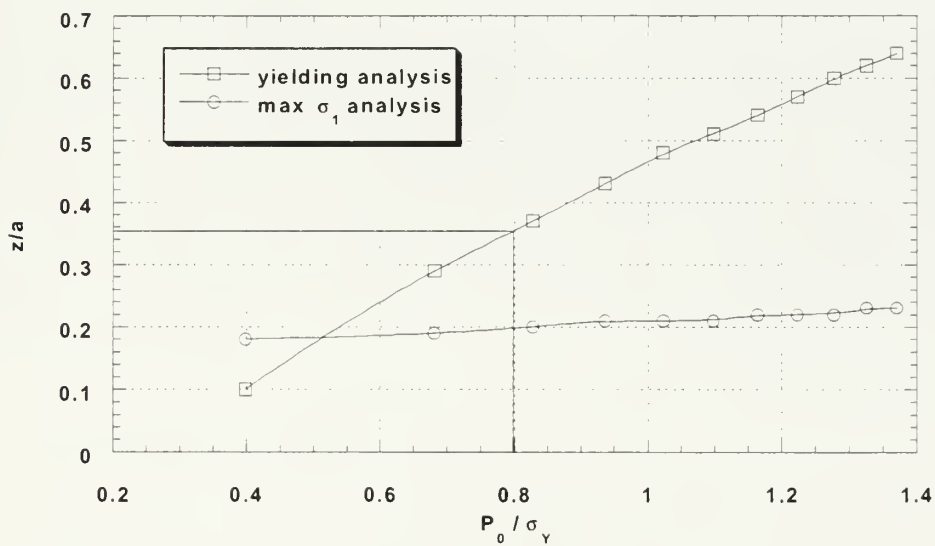


Figure 5-14: Optimum peening depth plotted versus maximum contact pressure for $\mu = 0.8$, $\sigma_b = 0.1\sigma_Y$.

Parameter	Value
ΔK_0	3 MPa $\sqrt{\text{m}}$
R	0.1
a	50 μm
Y	1

Table 5.1: Parameters and respective values for the threshold stress intensity range analysis.

5.3 Stress Intensity Range Threshold Analysis

The maximum principal stress analysis is a conservative approach. An alternative to the maximum principal analysis is an analysis based on the threshold stress intensity factor range ΔK_0 . At stress intensity factor ranges below the threshold, cracks either remain dormant or grow at undetectable rates [24]. This could be used in place of the maximum principal stress analysis to determine the optimum peening depth. Using the values listed in Table 5.1, a MATLAB script file was written to determine the peening depth such that $\Delta K_{\text{applied}} < \Delta K_0$. The expression used for $\Delta K_{\text{applied}}$ is given by:

$$\Delta K_{\text{applied}} = Y(\Delta\sigma)\sqrt{\pi a} \quad (5.3)$$

where Y is a geometrical factor.

The analysis was performed using $\sigma_b = 0.6\sigma_Y$, and $\mu = 0.8$. The material stresses in the x -direction were used to determine $\Delta\sigma$. Figure 5-15 shows the results of the analysis, where the required peening depth is plotted versus the maximum contact pressure. In this figure the results of the maximum principal stress analysis for the same loading conditions are also given for comparison. As can be seen in the figure, the maximum principal stress analysis is the more conservative analysis.

5.4 Protective Coatings

The protective coatings analysis in this work focuses on the ability of the coating to change the coefficient of friction of the system. Again a sphere on flat plane geometry is used in this section. A change in the coefficient of friction has a direct impact on the contact stresses. The contact stresses displayed in Equations 2.10 and 2.11 are shown again below in Equations 5.4

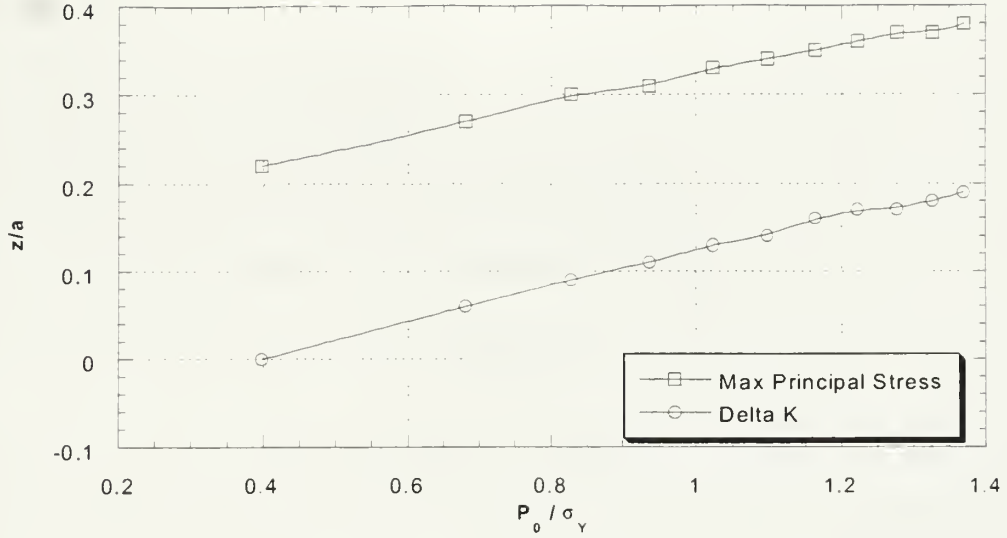


Figure 5-15: Comparison of the required peening depths for the maximum principal stress analysis and the threshold stress intensity range analysis.

and 5.5. The stresses at the edge of contact, at the surface, are given by:

$$\sigma_x = P_0 \left[\frac{(1 - 2\nu)}{3} \pm \frac{4 + \nu}{8} \pi \mu \right], \quad x = \mp a, \text{ and} \quad (5.4)$$

$$\sigma_y = P_0 \left[\frac{(2\nu - 1)}{3} \pm \frac{3\pi\nu\mu}{8} \right], \quad x = \mp a. \quad (5.5)$$

Therefore, reducing the coefficient of friction from a value of 1.2 to 1.0 will reduce the stresses from $\sigma_x = 2.160P_0$ to $\sigma_x = 1.822P_0$ and $\sigma_y = 0.291P_0$ to $\sigma_y = 0.220P_0$, assuming $\nu = 0.3$. So it can be seen that changing the coefficient of friction has a significant impact on the stresses induced by contact and therefore, on the fretting fatigue life of the structure. Figure 5-5 also demonstrates the benefit of reducing the coefficient of friction. It must be remembered that the equations shown above were for global sliding conditions. However, Chivers and Gordelier in [16] have shown that for $\mu > 0.2$, reducing μ will also reduce stress for stick-slip conditions.

No experiments have been conducted as part of this work in which the coefficient of friction was purposely altered to examine the actual effect on fretting fatigue life. However, Chivers

and Gordelier [41] performed a number of experiments for various fretting fatigue palliatives including shot peening and protective coatings and their results do support the validity of the discussion above. They examined two types of non-metallic coatings. Both were graphite-filled resins, one of the resins was a polyimide and the other was an isocyanate epoxy. The improvements in fretting fatigue behavior produced by the coatings were quite significant and were observed at all stress levels. Chivers and Gordelier [41], define a term called the improvement factor, I_f , to measure the success of the various palliatives being investigated. I_f is given by:

$$I_f = \frac{\sigma_p - \sigma_f}{\sigma - \sigma_f} \quad (5.6)$$

where σ_p is the run-out stress under fretting conditions with a palliative, σ_f is the run-out stress under fretting conditions and no palliative and σ is the run-out stress without fretting. Chivers and Gordelier define the run-out stress as the stress at which failure does not occur in about 10^8 cycles. The improvement factor values were found to be $I_f = 0.3$ for graphite in polyimide resin and $I_f = 0.55$ for graphite in epoxy resin. For comparison purposes the improvement factors found for shot peening were $I_f = 0.47$ for low intensity peening and $I_f = 0.43$ for high intensity peening. It is interesting that the graphite in epoxy resin coating actually outperformed shot peening. Chivers and Gordelier also performed experiments using a copper shim and the combination of a copper shim and graphite in epoxy. The use of the copper shim was intended to reduce the contact stresses at the surface of the material due to fretting, which from the previous analysis, again should improve fretting fatigue behavior. The improvement factors found were $I_f = 0.63$ with copper shim and $I_f = 0.77$ using both a copper shim and graphite in epoxy. Flat ended cylindrical pads made of 1Cr-Mo steel were fretted against rectangular 3.5Ni-Cr-Mo-V specimens for the experiments conducted by Chivers and Gordelier in [41]. The reduction in fatigue life due to fretting is directly related to the stresses at the contact surface and if the stresses can be reduced the fatigue life will be improved.

Chapter 6

Conclusions and Future Work

6.1 Conclusions

The key findings in this work are summarized below.

- The surface stresses due to contact can be used to characterize the damaging effects of fretting on the fatigue properties of a material. The critical fretting parameters, such as: the normal contact load, the oscillating tangential load and the coefficient of friction are all incorporated into the expressions for the contact stresses. It was shown that for a given bulk loading condition, the fretting fatigue life is reduced as the effective contact stresses are increased.
- A fretting fatigue knock-down factor curve has been produced for Al 7075-T6. It shows the approximate relationship between the effective stress due to contact and the magnitude of the fretting fatigue knock-down factor, KF .
- It was shown that the use of a single correction factor to modify the Basquin relationship for fretting fatigue would require extensive experimental work. The correction factor can be expressed as a function of the effective stress due to contact for a given bulk loading condition. However, this relationship changes as the bulk loading is changed. Therefore, families of correction factor curves would need to be developed for various bulk loadings. The experimental work required may be tenable if the correction factor was determined

to be a function of the contact stresses only and not dependent on the contact geometry for a given material.

- A failure envelope curve has been generated for Al 7075-T6. This curve shows the approximate combination of bulk and contact loading that will produce component failure.
- The damage tolerant approach analysis has been used to bound the crack initiation and short crack propagation stages of fretting fatigue.
- A new method has been proposed to determine the optimum peening depth for a component that undergoes fretting using the stress analysis provided by Hamilton [14]. The method was applied to a sphere on flat surface contact geometry, but is valid for any contact geometry that has analytic expressions for the stress fields. The optimum peening depth has been determined for Ti-6Al-4V for various combinations of bulk and contact loadings, for a given coefficient of friction. This analysis was performed for four different values of the coefficient of friction, so that the effect of coatings on peening depth could be analyzed.

6.2 Future Work

More experimental work needs to be performed to determine a more accurate failure envelope curve. This could prove to be a very beneficial design tool, especially if it was shown to be geometry independent. Theoretical work is also needed for this curve to better understand why the given combination of contact and bulk stresses lead to component failure. This will require a thorough examination of the crack initiation stage of fretting fatigue crack growth.

The shot peening analysis provided in this work also needs experimental validation to determine the actual depth of mechanical stress relieving due to the contact stresses. If the compressive residual stresses due to shot peening are relieved, the damage to the surface by the shot peening process may cause a significant reduction in the fatigue strength of the material as was discussed earlier.

More experimental work also needs to be done to determine the exact location of crack initiation. The pictures displayed in the previous work do not provide conclusive evidence for

the location of crack initiation. Interrupted tests are recommended because they could provide not only the location of crack initiation, but could also provide information on the number of cycles required for crack initiation. More analysis is also required for the predicted location of crack initiation for fretted components. The stress analysis approach does not always predict the correct location of crack initiation.

Appendix A

Ti-6Al-4V Yielding Analysis Program

```
%Ti-6Al-4V Yielding Analysis
```

```
%Input the material properties
```

```
E=115.7e9;
```

```
nu=0.321;
```

```
R=12.7e-3;
```

```
Sy=925e6;
```

```
K=3*(1-nu^2)/(2*E);
```

```
Sres=-0.85*Sy
```

```
Saxial=-.1*Sy
```

```
%Where E:Young's Modulus, nu:Poisson's Ratio, R:Radius of fretting pads.
```

```
%Sy:Yield Strength, Sres:Residual Stress, Saxial:Applied bulk stress
```

```
for jj=1:8
```

```
mu=0.5;
```

```
for k=1:6
```

```
P=0.20;
```

```
Ry=0;
```

```
% Increase the contact load, P, for each mu and Saxial until the effective
```



```

% stress exceeds Sy.
while Ry<1
a=(K*P*R)^(1/3);
Po=(3*P)/(2*pi*a^2);
B1=Po/a;
B2=mu*B1;
%Input Hamilton's Equations
y=0;
z(1)=0.0000001*a;
x(1)=-1.05*a;
for j=1:1
for i=1:110
r=x(i);
A=(r^2)+(z(j)^2)-(a^2);
S=((A^2)+(4*(a^2)*(z(j)^2)))^(1/2);
M=((S+A)/2)^(1/2);
N=((S-A)/2)^(1/2);
phi=atan(a/M);
G=(M^2)-(N^2)+(z(j)*M)-(a*N);
H=(2*M*N)+(a*M)+(z(j)*N);
%Stresses due to normal loads
Sxn=(Po/a)*((1+nu)*z(j)*phi+(1/r^2)*((0-x(i)^2/r^2)*((1-nu)*N*z(j)^2-
((1-2*nu)/3)*(N*S+2*A*N+a^3)-nu*M*z(j)*a)-N*(x(i)^2)-(M*x(i)^2*z(j)*a/S)));
Syn=(Po/a)*((1+nu)*z(j)*phi+(1/r^2)*((x(i)^2/r^2)*((1-nu)*N*z(j)^2-((1-2*nu)/3)
*(N*S+2*A*N+a^3)-nu*M*z(j)*a)-N*(2*nu*x(i)^2)-(0/S)));
Szn=B1*(-N+(a*z(j)*M)/S);
TAzxn=B1*(-z(j)*(x(i)*N/S-(x(i)*z(j)*H/(G^2+H^2))));
%Stresses due to tangential loads
Sxt=B2*(-x(i)*(nu/4+1)*phi+(a*x(i)*M/r^4)*((3/2-2*x(i)^2/r^2)*(S^nu-2*A^nu+
z(j)^2)+(x(i)^2*z(j)^2/S)+(7*nu*r^2/4)-(2*nu*x(i)^2)+r^2)+(x(i)*z(j)*N/r^4)*

```



```

((3/2-2*x(i)^2/r^2)*(-S/6*(1-2*nu)-A/3*(1-2*nu)-.5*(z(j)^2+3*a^2))+
(a^2*x(i)^2/S)-(nu*r^2/4)-(7*r^2/4))+(4*a^3*x(i)*z(j)/(3*r^4))*
(3/2-2*x(i)^2/r^2)*(1-2*nu));
Syt=B2*((-3*nu*x(i)*phi/4)+(a*x(i)*M/r^4)*((1/2-2*0/r^2)*(S*nu-2*A*nu+z(j)^2+
r^2*nu)+(0*z(j)^2/S)+(3*nu*r^2/4)))+(x(i)*z(j)*N/r^4)*((1/2-2*0/r^2)*
(-S/6*(1-2*nu)-A/3*(1-2*nu)-.5*(z(j)^2+3*a^2)))+(a^2*0/S)-(3*nu*r^2/4)-(1*r^2/4))+
(4*a^3*x(i)*z(j)/(3*r^4))*(1/2-2*0/r^2)*(1-2*nu));
Szt=B2*((z(j)*x(i)*N/(2*r^2)*(1-(r^2+z(j)^2+a^2)/S)));
TAzxt=B2*((3*z(j)*phi/2)+(a*z(j)*M/r^2)*(1+x(i)^2/r^2-x(i)^2/S)+N/r^2*
(-.75*(S+2*A)+z(j)^2-.75*a^2-.25*r^2+z(j)^2/2*(.5-2*x(i)^2/r^2)));
%Now combine the stresses
Sxtot=Sxn+Sxt+Sres+Saxial;
Sytot=Syn+Syt+Sres;
Sztot=Szn+Szt;
TAzxtot=TAzxn+TAzxt;
%Determine J2 and von Mises effective stress
J2=1/6*((Sxtot-Sytot)^2+(Sytot-Sztot)^2+(Sztot-Sxtot)^2)+TAzxtot^2;
H2=J2^.5;
Se(i,j)=3^.5*H2;
x(i+1)=x(i)+.02*a;
end
z(j+1)=z(j)+.025*a;
end
[Sem,i]=max(Se);
x1=x/a;
x1=x1';
z1=z';
z1=z1/a;
Se=Se;
%Now give x,z location of max stress

```



```

[Smm,zm]=max(Sem);
znm=z(zm);
zma=znm/a;
xm=i(zm);
xmm=x(xm);
xma=xmm/a;
%Now find the stresses at x=a, and x=-a at the surface
a=(K*P*R)^(1/3);
Po=(3*P)/(2*pi*a^2);
B1=Po/a;
B2=mu*B1;
x2=-a;
r=x2;
Sxtna=B2*(-pi*x2/2*((nu/4)+1));
Sytna=B2*(-3*pi*nu*x2/8);
Sxnna=B1*((1-2*nu)*a/3);
Synna=B1*((1-2*nu)*(-a/3));
Sxtona=Sxtna+Sxnna+Sres+Saxial;
Sytona=Sytna+Synna+Sres;
J2na=1/6*((Sxtona-Sytona)^2+(Sytona-0)^2+(0-Sxtona)^2)+0^2;
H2na=J2na^.5;
Sena=3^.5*H2na;
%Find stresses at x=a
x2=a;
r=x2;
Sxtpa=B2*(-pi*x2/2*((nu/4)+1));
Sytpa=B2*(-3*pi*nu*x2/8);
Sxnpa=B1*((1-2*nu)*a/3);
Synpa=B1*((1-2*nu)*(-a/3));
SxtoPa=Sxtpa+Sxnpa+Sres+Saxial;

```



```

SytoPa=Sytpa+Synpa+Sres;
J2pa=1/6*((SxtoPa-SytoPa)^2+(SytoPa-0)^2+(0-SxtoPa)^2)+0^2;
H2pa=J2pa^.5;
Sepa=3^.5*H2pa;
%Now determine the maximum effective stress
Smmm=[Simm,Sena,Sepa]
[Smmmax,xmmax]=max(Smmm);
Semax=Simmmax;
Ry=Semax/Sy;
P=P+.2;
end
P1=P-.2;
P2(k,jj)=P1;
mu=mu+.1;
end
Saxial=Saxial+(.1*Sy)
end
mu=mu;
P2=P2
%Now put P terms over yield strength.
for n=1:8
for i=1:6
a=(K*P2(i,n)*R)^(1/3);
Pol(i,n)=(3*P2(i,n))/(2*pi*a^2);
Ryy(i,n)=Pol(i,n)/Sy;
end
end
Ryy=Ryy

```


Appendix B

Depth of Yielding Analysis

%Ti-6Al-4V Depth of Yielding Analysis

%Input the material properties

E=115.7e9;

nu=0.321;

R=12.7e-3;

Sy=925e6;

K=3*(1-nu^2)/(2*E);

Sres=-.85*Sy

mu=0.3;

Saxial=-0.1*Sy

for jj=1:4

P=10;

for k=1:2

a=(K*P*R)^(1/3);

Po=(3*P)/(2*pi*a^2);

B1=Po/a;

B2=mu*B1;

%Input Hamilton's Equations

y=0;

z(1)=0.0000001*a;


```

x(1)=-1.05*a;
for j=1:27
for i=1:110
r=x(i);
A=(r^2)+(z(j)^2)-(a^2);
S=((A^2)+(4*(a^2)*(z(j)^2)))^(1/2);
M=((S+A)/2)^(1/2);
N=((S-A)/2)^(1/2);
phi=atan(a/M);
G=(M^2)-(N^2)+(z(j)*M)-(a*N);
H=(2*M*N)+(a*M)+(z(j)*N);
%STRESSES DUE TO NORMAL LOADS
Sxn=(Po/a)*((1+nu)*z(j)*phi+(1/r^2)*((0-x(i)^2/r^2)*((1-nu)*N*z(j)^2-
((1-2*nu)/3)*(N*S+2*A*N+a^3)-nu*M*z(j)*a)-N*(x(i)^2)-(M*x(i)^2*z(j)*a/S)));
Syn=(Po/a)*((1+nu)*z(j)*phi+(1/r^2)*((x(i)^2/r^2)*((1-nu)*N*z(j)^2-
((1-2*nu)/3)*(N*S+2*A*N+a^3)-nu*M*z(j)*a)-N*(2*nu*x(i)^2)-(0/S)));
Szn=B1*(-N+(a*z(j)*M)/S);
TAzxn=B1*(-z(j)*(x(i)*N/S-(x(i)*z(j)*H/(G^2+H^2))));
%Stresses due to tangential loads
Sxt=B2*(-x(i)*(nu/4+1)*phi+(a*x(i)*M/r^4)*((3/2-2*x(i)^2/r^2)*
(S*nu-2*A*nu+z(j)^2)+(x(i)^2*z(j)^2/S)+(7*nu*r^2/4)-(2*nu*x(i)^2)+r^2)+
(x(i)*z(j)*N/r^4)*((3/2-2*x(i)^2/r^2)*(-S/6*(1-2*nu)-A/3*(1-2*nu)-
.5*(z(j)^2+3*a^2)))+(a^2*x(i)^2/S)-(nu*r^2/4)-(7*r^2/4))+
(4*a^3*x(i)*z(j)/(3*r^4))*(3/2-2*x(i)^2/r^2)*(1-2*nu));
Syt=B2*((-3*nu*x(i)*phi/4)+(a*x(i)*M/r^4)*((1/2-2*0/r^2)*
(S*nu-2*A*nu+z(j)^2+r^2*nu)+(0*z(j)^2/S)+(3*nu*r^2/4)))+(x(i)*z(j)*N/r^4)*
((1/2-2*0/r^2)*(-S/6*(1-2*nu)-A/3*(1-2*nu)-.5*(z(j)^2+3*a^2)))+(a^2*0/S)-
(3*nu*r^2/4)-(1*r^2/4)))+(4*a^3*x(i)*z(j)/(3*r^4))*(1/2-2*0/r^2)*(1-2*nu));
Szt=B2*((z(j)*x(i)*N/(2*r^2)*(1-(r^2+z(j)^2+a^2)/S)));
TAzxt=B2*((3*z(j)*phi/2)+(a*z(j)*M/r^2)*(1+x(i)^2/r^2-x(i)^2/S)+N/r^2*

```



```

(-.75*(S+2*A)+z(j)^2-.75*a^2-.25*r^2+z(j)^2/2*(.5-2*x(i)^2/r^2)));
%Now combine the stresses
Sxtot=Sxn+Sxt+Sres+Saxial;
Sytot=Syn+Syt+Sres;
Sztot=Szn+Szt;
TAzxtot=TAzxn+TAzxt;
%Determine J2 and von Mises effective stress
J2=1/6*((Sxtot-Sytot)^2+(Sytot-Sztot)^2+(Sztot-Sxtot)^2)+TAzxtot^2;
H2=J2^.5;
Se(i,j)=3^.5*H2;
x(i+1)=x(i)+.02*a;
end
z(j+1)=z(j)+.02*a;
end
[Sem,i]=max(Se);
x1=x/a;
x1=x1';
z12=z';
z13=z12/a;
Se=Se;
%Now give x,z location of max stress
[Simm,zm]=max(Sem);
zmm=z(zm);
zma=zmm/a;
xm=i(zm);
xmm=x(xm);
xma=xmm/a;
%Now determine when von Mises effective stress equals yield stress
Ry=2;
zma=zma

```



```

z1=zma*a;
x1(1)=-1.05*a;
while Ry>1
for i=1:110
a=(K*P*R)^(1/3);
Po=(3*P)/(2*pi*a^2);
B1=Po/a;
B2=mu*B1;
r=x1(i);
A=(r^2)+(z1^2)-(a^2);
S=((A^2)+(4*(a^2)*(z1^2)))^(1/2);
M=((S+A)/2)^(1/2);
N=((S-A)/2)^(1/2);
phi=atan(a/M);
G=(M^2)-(N^2)+(z1*M)-(a*N);
H=(2*M*N)+(a*M)+(z1*N);
%Stresses due to normal loads
Sxn=(Po/a)*((1+nu)*z1*phi+(1/r^2)*((0-x1(i)^2/r^2)*((1-nu)*N*z1^2-
((1-2*nu)/3)*(N*S+2*A*N+a^3)-nu*M*z1*a)-N*x1(i)^2-(M*x1(i)^2*z1*a/S)));
Syn=(Po/a)*((1+nu)*z1*phi+(1/r^2)*((x1(i)^2/r^2)*((1-nu)*N*z1^2-
((1-2*nu)/3)*(N*S+2*A*N+a^3)-nu*M*z1*a)-N*(2*nu*x1(i)^2)-(0/S)));
Szn=B1*(-N+(a*z1*M)/S);
TAzxn=B1*(-z1*(x1(i)*N/S-(x1(i)*z1*H/(G^2+H^2))));
%Stresses due to tangential loads
Sxt=B2*(-x1(i)*(nu/4+1)*phi+(a*x1(i)*M/r^4)*((3/2-2*x1(i)^2/r^2)*
(S*nu-2*A*nu+z1^2)+(x1(i)^2*z1^2/S)+(7*nu*r^2/4)-(2*nu*x1(i)^2)+r^2)+
(x1(i)*z1*N/r^4)*((3/2-2*x1(i)^2/r^2)*(-S/6*(1-2*nu)-A/3*(1-2*nu)-.5*
(z1^2+3*a^2)))+(a^2*x1(i)^2/S)-(nu*r^2/4)-(7*r^2/4)))+(4*a^3*x1(i)*z1/(3*r^4))*
(3/2-2*x1(i)^2/r^2)*(1-2*nu));
Syt=B2*((-3*nu*x1(i)*phi/4)+(a*x1(i)*M/r^4)*((1/2-2*0/r^2)*(S*nu-2*A*nu+z1^2+

```



```

r^2*nu)+(0*z1^2/S)+(3*nu*r^2/4))+(x1(i)*z1*N/r^4)*((1/2-2*0/r^2)*(-S/6*
(1-2*nu)-A/3*(1-2*nu)-.5*(z1^2+3*a^2)))+(a^2*0/S)-(3*nu*r^2/4)-(1*r^2/4))+
(4*a^3*x1(i)*z1/(3*r^4))*(1/2-2*0/r^2)*(1-2*nu));
Szt=B2*((z1*x1(i)*N/(2*r^2)*(1-(r^2+z1^2+a^2)/S)));
TAzxt=B2*((3*z1*phi/2)+(a*z1*M/r^2)*(1+x1(i)^2/r^2-x1(i)^2/S)+N/r^2*
(-.75*(S+2*A)+z1^2-.75*a^2-.25*r^2+z1^2/2*(.5-2*x1(i)^2/r^2)));
%Now combine the stresses
Sxtot=Sxn+Sxt+Sres+Saxial;
Sytot=Syn+Syt+Sres;
Sztot=Szn+Szt;
TAzxtot=TAzxn+TAzxt;
%Determine J2 and von Mises equivalent stress
J2=1/6*((Sxtot-Sytot)^2+(Sytot-Sztot)^2+(Sztot-Sxtot)^2)+TAzxtot^2;
H2=J2^.5;
Se1(i)=3^.5*H2;
x1(i+1)=x1(i)+.02*a;
end
Sem1=max(Se1);
Ry=Sem1/Sy
z1=z1+.01*a;
end
z11(k,jj)=(z1/a)-.01;
P=P+40;
end
Saxial=Saxial+.1*Sy
end
z11=z11
mu=mu;

```


Appendix C

Maximum Principal Stress Analysis

%Ti-6Al-4V Maximum Principal Stress Analysis

%Input the material properties

E=115.7e9;

nu=0.321;

R=12.7e-3;

Sy=925e6;

mu=0.30;

K=3*(1-nu^2)/(2*E);

Sres=-.85*Sy;

Saxial=-.1*Sy;

for cc=1:8

P=10;

for k=1:11

S1max=1;

a=(K*P*R)^(1/3);

Po=(3*P)/(2*pi*a^2);

B1=Po/a;

B2=mu*B1;

%Input Hamilton's Equations

y=0;


```

z=0.0000001*a;
x(1)=-1.05*a;
while S1max>0
%S1max is the maximum principal stress
for i=1:110
r=x(i);
A=(r^2)+(z^2)-(a^2);
S=((A^2)+(4*(a^2)*(z^2)))^(1/2);
M=((S+A)/2)^(1/2);
N=((S-A)/2)^(1/2);
phi=atan(a/M);
G=(M^2)-(N^2)+(z*M)-(a*N);
H=(2*M*N)+(a*M)+(z*N);
%STRESSES DUE TO NORMAL LOADS
Sxn=(Po/a)*((1+nu)*z*phi+(1/r^2)*((0-x(i)^2/r^2)*((1-nu)*N*z^2-
((1-2*nu)/3)*(N*S+2*A*N+a^3)-nu*M*z*a)-N*(x(i)^2)-(M*x(i)^2*z*a/S)));
Syn=(Po/a)*((1+nu)*z*phi+(1/r^2)*((x(i)^2/r^2)*((1-nu)*N*z^2-
((1-2*nu)/3)*(N*S+2*A*N+a^3)-nu*M*z*a)-N*(2*nu*x(i)^2)-(0/S)));
Szn=B1*(-N+(a*z*M)/S);
TAzxn=B1*(-z*(x(i)*N/S-(x(i)*z*H/(G^2+H^2))));
%Stresses due to tangential loads
Sxt=B2*(-x(i)*(nu/4+1)*phi+(a*x(i)*M/r^4)*((3/2-2*x(i)^2/r^2)*
(S*nu-2*A*nu+z^2)+(x(i)^2*z^2/S)+(7*nu*r^2/4)-(2*nu*x(i)^2)+r^2)+
(x(i)*z*N/r^4)*((3/2-2*x(i)^2/r^2)*(-S/6*(1-2*nu)-A/3*(1-2*nu)-
.5*(z^2+3*a^2)))+(a^2*x(i)^2/S)-(nu*r^2/4)-(7*r^2/4)))+(4*a^3*x(i)*
z/(3*r^4))*(3/2-2*x(i)^2/r^2)*(1-2*nu));
Syt=B2*((-3*nu*x(i)*phi/4)+(a*x(i)*M/r^4)*((1/2-2*0/r^2)*
(S*nu-2*A*nu+z^2+r^2*nu)+(0*z^2/S)+(3*nu*r^2/4)))+(x(i)*z*N/r^4)*
((1/2-2*0/r^2)*(-S/6*(1-2*nu)-A/3*(1-2*nu)-.5*(z^2+3*a^2))+
(a^2*0/S)-(3*nu*r^2/4)-(1*r^2/4)))+(4*a^3*x(i)*z/(3*r^4))*

```



```

(1/2-2*0/r^2)*(1-2*nu));
Szt=B2*((z*x(i)*N/(2*r^2)*(1-(r^2+z^2+a^2)/S)));
TAzxt=B2*((3*z*phi/2)+(a*z*M/r^2)*(1+x(i)^2/r^2-x(i)^2/S)+
N/r^2*(-.75*(S+2*A)+z^2-.75*a^2-.25*r^2+z^2/2*(.5-2*x(i)^2/r^2)));
%Now combine the stresses
Sxtot=Sxn+Sxt+Sres+Saxial;
Sytot=Syn+Syt+Sres;
Sztot=Szn+Szt;
TAzxtot=TAzxn+TAzxt;
Sxtotv(i)=Sxtot;
Sztotv(i)=Sztot;
TAzxtotv(i)=TAzxtot;
%Determine the max principal stress for each point
cxz=(Sxtot+Sztot)/2;
rxz=((Sxtot-cxz)^2+TAzxtot^2)^.5;
S1xz(i)=cxz+rxz;
x(i+1)=x(i)+.02*a;
end
%Find the maximum principal stress of the vector of principal stresses
S1xzm=max(S1xz);
Sxmax=max(Sxtotv);
Szmax=max(Sztotv);
TAzxmax=max(TAzxtotv);
S1max=S1xzm
z=z+.01*a;
zaa=z/a
end
z2(k,cc)=z-.01*a;
a=a;
z3(k,cc)=(1/a)*z2(k,cc);

```



```
P=P+40
```

```
end
```

```
Saxial=Saxial+.1*Sy
```

```
end
```

```
z2=z2
```

```
z3=z3
```

```
mu=mu;
```


Appendix D

Hamilton's Expressions

D.1 Normal Load Stresses

$$\sigma_x = \frac{3P}{2\pi a^3} \left[(1 + \nu) z\phi + \frac{1}{r^2} \left\{ \frac{y^2 - x^2}{r^2} \left[(1 - \nu) Nz^2 - \frac{1 - 2\nu}{3} (NS + 2AN + a^3) - \nu Mza \right] - N(x^2 + 2\nu y^2) - \frac{Mx^2za}{S} \right\} \right]$$

$$\sigma_y = \frac{3P}{2\pi a^3} \left[(1 + \nu) z\phi + \frac{1}{r^2} \left\{ \frac{x^2 - y^2}{r^2} \left[(1 - \nu) Nz^2 - \frac{1 - 2\nu}{3} (NS + 2AN + a^3) - \nu Mza \right] - N(y^2 + 2\nu x^2) - \frac{My^2za}{S} \right\} \right]$$

$$\sigma_z = \frac{3P}{2\pi a^3} \left[-N + \frac{azM}{S} \right]$$

At $y = 0$, the only non-zero shear stress is τ_{zx} .

$$\tau_{zx} = \frac{3P}{2\pi a^3} \left[-z \left\{ \frac{xN}{S} - \frac{xzH}{G^2 + H^2} \right\} \right]$$

where

$$A = r^2 + z^2 - a^2; \quad S = (A^2 + 4a^2z^2)^{1/2}; \quad r^2 = x^2 + y^2 \text{ and} \\ M = \left(\frac{S+A}{2} \right)^{1/2}; \quad N = \left(\frac{S-A}{2} \right)^{1/2}; \quad \phi = \tan^{-1} \left(\frac{a}{M} \right) \text{ and}$$

$$G = M^2 - N^2 + zM - aN; \quad H = 2MN + aM + zN$$

On the axis where $r = 0$, the formulae above are indeterminate and must be re-worked.

Hamilton performed this and the expressions are now given by:

$$\sigma_x = \sigma_y = \frac{3P}{2\pi a^3} \left[(1 + \nu) (z \tan^{-1} (a/z) - a) + \frac{a^3}{2(a^2 + z^2)} \right]$$

$$\sigma_z = \frac{3P}{2\pi a^3} \left[\frac{-a^3}{a^2 + z^2} \right]$$

$$\text{and } \tau_{xy} = \tau_{yz} = \tau_{zx} = 0.$$

D.2 Tangential Load Stresses

$$\sigma_x = \frac{3Q}{2\pi a^3} \left[\begin{aligned} & -x \left(\frac{\nu}{4} + 1 \right) \phi + \frac{axM}{r^4} \left\{ \left(\frac{3}{2} - \frac{2x^2}{r^2} \right) (S\nu - 2A\nu + z^2) + \frac{x^2 z^2}{S^2} + \frac{7\nu r^2}{4} - 2\nu x^2 + r^2 \right\} \\ & + \frac{xzN}{r^4} \left\{ \left(\frac{3}{2} - \frac{2x^2}{r^2} \right) \left[-\frac{S}{6} (1 - 2\nu) - \frac{A}{3} (1 - 2\nu) - \frac{1}{2} (z^2 + 3a^2) \right] + \frac{a^2 x^2}{S} - \frac{\nu r^2 + 7r^2}{4} \right\} \\ & + \frac{4a^3 xz}{3r^4} \left(\frac{3}{2} - \frac{2x^2}{r^2} \right) (1 - 2\nu) \end{aligned} \right]$$

$$\sigma_y = \frac{3Q}{2\pi a^3} \left[\begin{aligned} & -\frac{3\nu x\phi}{4} + \frac{axM}{r^4} \left\{ \left(\frac{1}{2} - \frac{2y^2}{r^2} \right) [(S\nu - 2A\nu + r^2\nu) + z^2] + \frac{y^2 z^2}{S} + \frac{3\nu r^2}{4} \right\} \\ & + \frac{xzN}{r^4} \left\{ \left(\frac{1}{2} - \frac{2y^2}{r^2} \right) \left[-\frac{S}{6} (1 - 2\nu) - \frac{A}{3} (1 - 2\nu) - \frac{1}{2} (z^2 + 3a^2) \right] + \frac{a^2 y^2}{S} - \frac{3\nu r^2 + r^2}{4} \right\} \\ & + \frac{4a^3 xz}{3r^4} \left(\frac{1}{2} - \frac{2y^2}{r^2} \right) (1 - 2\nu) \end{aligned} \right]$$

Again the only non-zero shear stress at $y = 0$ is τ_{zx} .

* Note the equation for σ_x in the original paper by Hamilton contained an error. The paper contained the number 3 in the expression marked above where it should have contained an S . The units do not work if this change is not made.

$$\tau_{zx} = \frac{3Q}{2\pi a^3} \left[\frac{3z\phi}{2} + \frac{azM}{r^2} \left\{ 1 + \frac{x^2}{r^2} - \frac{x^2}{S} \right\} + \frac{N}{r^2} \left\{ \begin{aligned} & -\frac{3}{4} (S + 2A) + z^2 - \frac{3a^2 + r^2}{4} \\ & + \frac{z^2}{2} \left(\frac{1}{2} - \frac{2x^2}{r^2} \right) \end{aligned} \right\} \right]$$

Bibliography

- [1] NMAB Committee on Control of Fretting-Initiated Fatigue, Control of Fretting Fatigue, NMAB-333, National Academy of Sciences, Washington, D.C., 1977.
- [2] Hattori, T., Fretting Fatigue Problems in Structural Design, *Fretting Fatigue*, ESIS 18 (Edited by Waterhouse, R. B. and Lindley, T.C.) 1994, Mechanical Engineering Publications, 437-451.
- [3] Eden, E.M., Rose, W.N., and Cunningham, F.L., Then Endurance of Metals, *Proc. Inst. Mech. Engrs*, 1911,
- [4] Heoppner, D.W., Mechanisms of Fretting Fatigue, *Fretting Fatigue*, ESIS 18 (Edited by Waterhouse, R. B. and Lindley, T.C.) 1994, Mechanical Engineering Publications, 3-19.
- [5] Warlow-Davies, E.J., Fretting Corrosion and Fatigue Strength: Brief Results of Preliminary Experiments, *Proc. Inst. Mech. Engrs. 1941*, **146**, 32-38.
- [6] Edwards, R.P., The Application of Fracture Mechanics to Predicting Fretting Fatigue, *Fretting Fatigue*, (Edited by Waterhouse, R.B.), 1981, Applied Science Publishers LTD London, 67-97.
- [7] Faanes, S. and Fernando, U.S., Life Prediction in Fretting Fatigue using Fracture Mechanics, *Fretting Fatigue*, ESIS 18 (Edited by Waterhouse, R. B. and Lindley, T.C.) 1994, Mechanical Engineering Publications, London 149-159.
- [8] Bannantine, J.A., Comer, J.J. and Handrock, J.L., *Fundamentals of Metal Fatigue Analysis*, Prentice-Hall, Englewood Cliffs, NJ, 1990.

- [9] Waterhouse, R.B., Theories of Fretting Processes, *Fretting Fatigue*. (Edited by Waterhouse, R.B.), 1981, Applied Science Publishers LTD London, 203-219.
- [10] Nishioka, K. and Hirakawa, K., Fundamental Investigation of Fretting Fatigue -Part 5, The Effect of Relative Slip Amplitude, *Bull. J.S.M.E.*, 1969, **12**, 692-697.
- [11] Birch, P.R., A Study of Fretting Fatigue in Aircraft Components, Masters of Science Thesis, Massachusetts Institute of Technology (1998).
- [12] Conner, B.P. Thesis work in progress, Massachusetts Institute of Technology.
- [13] Hamilton, G.M. and Goodman, L.E., The Stress Field Created by a Circular Sliding Contact, *J. App. Mech.*, 1966, **33**, 371-376.
- [14] Hamilton, G.M., Explicit Equations for the Stresses Beneath a Sliding Spherical Contact, *Proc. Inst. Mech. Engrs.*, 1983, **197C**, 53-59.
- [15] Adibnazari, S. and Heoppner, D.W., The Role of Normal Pressure in Modelling Fretting Fatigue, *Fretting Fatigue*, ESIS 18 (Edited by Waterhouse, R. B. and Lindley, T.C.) 1994, Mechanical Engineering Publications, London 125-133.
- [16] Chivers, T.C. and Gordelier, S.C., Fretting fatigue and contact conditions: a rational explanation of palliative behavior, *Proc. Inst. Mech. Engrs.*, 1985, **199**, 325-337
- [17] Hertz, H., On the contact of elastic solids, *J. Reine und Angewandte Mathematik*, 1882, **92**, 156-171.
- [18] Huber, M.T. On the Theory of Elastic Solid Contact, *Annln. Phys. Lpz.*, 1904, **14**, 153-163.
- [19] Mindlin, R.D., Compliance of Elastic Bodies in Contact, *J. Appl. Mech.*, 1949, **16**, 259-268.
- [20] Mindlin, R.D. and Deresiewicz, H., Elastic Spheres in Contact Under Varying Oblique Forces, *J. App. Mech.*, **20**, 1953, 327-344.
- [21] Giannakopoulos, A.E., and Suresh, S., A Three-Dimensional Analysis of Fretting Fatigue, *Acta Materialia et Metalurgica*, 1998, **46**, 177-192.
- [22] Fuchs, H.O. and Stephens, R.I., *Metal Fatigue in Engineering*, Wiley, New York (1980).

- [23] Wittowsky, B.U., Birch, P.R., Dominguez, J., Suresh, S., An Experimental Investigation of Fretting Fatigue with Spherical Contact in 7075-T6 Aluminum Alloy, *Fretting Fatigue: Current Technology and Practices*, ASTM STP 1367, D.W. Heoppner, V. Chandrasekaran and C.B. Elliot, Eds., American Society for Testing Materials, 1999.
- [24] Suresh, S., *Fatigue of Materials*, Second Edition, Cambridge University Press, 1998.
- [25] Wittkowsky, B.U., Birch, P.R., Dominguez, J., and Suresh, S., An Apparatus for Quantitative Fretting-Fatigue Testing, Submitted to: *Fatigue and Fracture of Engineering Materials and Structures*, 1998.
- [26] Basquin, O.H., The Exponential Law of Endurance Tests. *Proceedings of the American Society for Testing and Materials*, 1910, **10**, 625-630.
- [27] Coffin, L.F., A Study of the Effects of Cyclic Thermal Stresses on a Ductile Metal. *Transactions of the American Society of Mechanical Engineers*, 1954, **76**, 931-950.
- [28] Manson, S.S., Behavior of materials under Conditions of Thermal Stress, *National Advisory Commission on Aeronautics: Report 1170*, 1954, Lewis Flight Propulsion Laboratory.
- [29] Waterhouse, R.B., Introduction to Fatigue, *Fretting Fatigue*, (Edited by Waterhouse, R.B.), 1981, Applied Science Publishers LTD London, 1-21.
- [30] Szolwinski, M.P. and Farris, T.N., Observation, Analysis and Prediction of Fretting Fatigue in 2024-T351 Aluminum Alloy, *Wear*, 1998, **221**, 24-36.
- [31] Paris, P.C., Gomez, M.P. and Anderson, W.P., A Rational Analytic Theory of Fatigue, *The Trend in Engineering*, 1961, **13**, 9-14.
- [32] Paris, P.C. and Erdogan, F., A critical analysis of crack propagation laws, *Journal of Basic Engineering*, 1963, **85**, 528-534.
- [33] Newman, J.C.,JR. and Raju, I.S., An Empirical Stress-Intensity Factor Equation for the Surface Crack. *Engineering Fracture Mechanics*, 1981, **15**, 185-192.
- [34] Meyers, M.A., Chawla, K.K., *Mechanical Metallurgy: Principles and Applications*, Prentice-Hall, 1984.

- [35] MCIC-HB-01R *Damage Tolerant Design Handbook. A Compilation of Fracture and Crack Growth Data for High-Strength Alloys*. Vol 4, BATTELE, Columbus, OH, 1983.
- [36] Boyce, B.L., Campbell, J.P., Roder, O., Thompson, A.W., Milligan, W.W., and Ritchie, R.O., Thresholds for High-Cycle Fatigue in a Turbine Engine Ti-6Al-4V Alloy, submitted to the *International Journal of Fatigue*, 1998.
- [37] *Materials Property Handbook: Titanium Alloys*. (Edited by Boyer, R., Welsch, G., Collings, E.W.), ASM International, 1994.
- [38] Waterhouse, R.B., Effect of Material and Surface Condition on Fretting Fatigue, *Fretting Fatigue*. ESIS 18 (Edited by Waterhouse, R. B. and Lindley, T.C.) 1994, Mechanical Engineering Publications, London 339-349.
- [39] Bignonnet, A., Some Observations of the Effect of Shot Peening on Fretting Fatigue, *Fretting Fatigue*, ESIS 18 (Edited by Waterhouse, R. B. and Lindley, T.C.) 1994, Mechanical Engineering Publications, London 475-482.
- [40] Morrow, J.D., *Fatigue Design Handbook-Advances in Engineering*. Warrendale, PA: Society of Automotive Engineers, 1968.
- [41] Chivers, T.C., Gordelier, S.C., Fretting Fatigue Palliatives: Some Comparative Experiments, *Wear*, 1984, **96**, 153-175.
- [42] Almen, J.O., and Black, P.H., *Residual Stresses and Fatigue in Metals*, McGraw-Hill, 1963.
- [43] Shot Peening Applications, Seventh Edition, Metal Improvement Company.
- [44] Gray, H., Wagner, L. and Lütjering, G., Influence of Shot Peening Induced Surface Roughness, Residual Macro stresses and Dislocation Density on the Elevated Temperature HCF-Properties of Ti alloys, *Shot Peening: Science-Technology-Application*, (Edited by Wohlfahrt, H., Kopp, R., Völhringer, O.), 1987, Deutsche Gesellschaft für Metallkunde e.V., 447-457.
- [45] MIL-HDBK-5G, *Metallic Materials and Elements for Aerospace Vehicle Structures*. Vol 2, Defense Printing Service Detachment Office, Philadelphia, PA, 1994.

- [46] Giannakopoulos, A.E., Lindley, T.C. and Suresh, S., Aspects of Equivalence Between Contact Mechanics and Fracture Mechanics: Theoretical Connections and a Life Prediction Methodology for Fretting Fatigue, *Acta Materialia*, 1998, **46**, 2955-2968.
- [47] Osgood, C.C., *Fatigue Design*, Second Edition, Pergamon Press, 1982.
- [48] Johnson, K. L., *Contact Mechanics*, Cambridge University Press, 1985.
- [49] O'Connor, J.J., The Role of Elastic Stress Analysis in the Interpretation of Fretting Fatigue Failures, *Fretting Fatigue*, (Edited by Waterhouse, R.B.), 1981, Applied Science Publishers LTD London, 23-66.
- [50] Waterhouse, R.B., Theories of Fretting Processes, *Fretting Fatigue*, (Edited by Waterhouse, R.B.), 1981, Applied Science Publishers LTD London, 203-219.

DUDLEY KNOX LIBRARY



3 2768 00402742 5